NASA ULI

Safe, Low-Noise Operation of UAM in Urban Canyons via Integration of Gust Outcomes and Trim Optimization

Annual Report, Year 1

Sheryl Grace, PI

Year 1, 8/23 - 8/24

Trustees of Boston University, 1 Silber Way, Boston, MA 02215-1703

Award Number: 80NSSC23M0057

Executive Summary

This ULI addresses NASA's ULI Strategic Thrust 4: Safe, Quiet, and Affordable Vertical Lift Air Vehicles. The main focus of the proposed research is the development of critical knowledge and prediction methods for addressing a main barrier to the development and adoption of Urban Air Mobility (UAM): *community noise*. The proposed project will enable the development of validated approaches to assist with the design of safe low-noise multirotor vehicles and control strategies for operation in urban settings. The developed methods will facilitate the investigation of potential UAM vertiport locations and flight corridors. The team is made up of researchers from Boston Univ., Embry Riddle Univ., Tuskegee Univ., Virginia Tech and Joby Aviation with educational partner Univ. of Maryland Eastern Shores.

This work supports ARMD's outcome for 2025-2035: New vertical lift configurations and technologies introduced that enable new markets, increase mobility, improve accessibility, and reduce environmental impact. The proposed research targets major outcome risks by improving the aeroacoustic modeling of UAM vehicles subject to environmental disturbances guiding both their future design and operation.

Research objectives and overall strategy

The requirements that UAM be safe like traditional aircraft, closer to carbon neutral than traditional aircraft, and provide vertical take-off and landing (VTOL) have driven designs that use multiple rotors. These vehicles come in a significant variety of configurations. A believed benefit is much quieter vehicles compared to traditional single large-rotor vehicles. However, UAM are expected to operate much closer to population centers on a more continuous basis than traditional aircraft. Furthermore, they will take off and land from rooftops that may be near other taller buildings and then fly in the urban canyon. The overarching objective of this research is to address fundamental knowledge gaps related to performance and noise that are critical for enabling UAM operation in an urban setting. To this end, the following activities are being undertaken to specifically address the followng technical challenges:

Technical challenges addressed

TC 1: *The effect of urban flows on UAM performance and noise.*

This is an expansive topic that has been largely unstudied previously. This project adopts a multipronged approach for addressing fundamental knowledge building blocks that support better understanding and prediction capabilities for multirotor vehicles in urban flows. This is a summary of the different inquiries and outcomes to date.

- Urban modeling
  - Single building urban flow modeling verified across PALM and OpenFOAM.
  - SPOD has been applied to single and multi-building configs to isolate disturbances of interest
  - Canonical multibuilding simulations with different wind directions are underway with mean and turbulence flow levels being compared
  - Disturbance characterization based on the simulation results continues

- Experimental campaign with single Joby prop
  - Design of 21% scale Joby prop and motor
  - Performance and noise measurements including source determination for single Joby prop: hover, advancing, edgewise; several blade pitch and flow speed cases
  - Design of actuator for disturbance generator
- Mid fidelity modeling
  - CHARM has been obtained and learned by the team; interactions with CDI have improved understanding of how to best run the software
  - Small APC props have been modeled using Xrotor and CHARM coupled to PSU-WOPWOP; performance for hover and advancing flight conditions have been validated against experimental data
  - Joby prop has been modeled in CHARM and initial comparisons with the experimental performance results obtained as part of this project show good agreement; noise results are still being analyzed
  - Airfoil tables have been developed based on local Reynolds number using XFOIL; the team has begun to utilize CFD capabilities for the development of improved airfoil tables
- High fidelity modeling
  - The AART experiment has been modeled using Helios with Overflow and validated against experiment
  - The 9x6E APC rotor downstream of cylinder has been simulated with OpenFOAM; performance has been validated; a reliable method for performing noise calculations with OpenFOAM is still being explored
  - Continued development of best practices for implementing permeable surface FWH
  - Joby prop with and without fairing has been modeled in both OpenFOAM and Helios. Accuracy of predictions is still being sorted out.

TC 2: *The effect of UAM trim state on performance and noise.*

This TC requires full vehicle performance and noise assessment as well as improved methods for trim determination. Much of this work is slated for years 2 and 3 but some progress has been made.

- An old database related to SUI Endurance quadrotor used to inform trim algorithm development is being revisited; noise is being included as a parameter; CHARM simulations of the SUI vehicle are underway
- To enable a real-time control algorithm, a new machine learning approach for obtaining the performance at a given state is being developed based on the SUI database; it can be extended to include noise as an output

TC 3: *The impact of noise as a metric on UAM path planning.*

Path planning algorithms that take into consideration noise as an additional metric do not exist, but may prove critical to gain community buy-in for UAM.

- The development of a path planning algorithm that depends on quantities integrated along its path as well as avoidance of specified metric levels is underway; the noise parameter currently being used is a simple amplitude decay function

Workforce development and dissemination.

- A successful outreach workshop was run at Virginia Tech May 20-24; 19 students were recruited from the participating universities as well as universities and colleges that serve a high population of minority students and schools with no graduate program
- Joby hosted 4 interns during summer of 2024 from the ULI schools
- "Evaluating the Permeable Surface Approach for Wing-Propeller Aeroacoustics using High-Fidelity CFD"; given by Adam Rozman; TVF, 2024, Santa Cruz, CA.
- "Acoustic predicts of UAM in real urban environments." Invited talk given by Sheryl Grace; NE VFS and BU student AIAA, March 2024.
- NASA ULI experimental findings: Aeroacoustics wind tunnel working session presentation given by Nathan Alexander, at Aeroacoustics, June 2024, Rome, Italy.
- "Characterizing Urban Flow Disturbances for Safe Urban Air Mobility (UAM) Operations using Large-Eddy Simulation," given by Emmanuel Akinlabi at Engineering Mechanics Institute and Probabilistic Mechanics & Reliability Conference, Chicago, Illinois, May 2024.
- "Characterizing Urban Flow Disturbances for Safe Urban Air Mobility (UAM) Operations using Large-Eddy Simulation," to be given by Dan Li at 2024 PALM Model Conference in Offenbach, Germany, Sept. 2024.
- "High-Fidelity Analysis of Unsteady Flow Characteristics Around Vertiport Model," given by Alireza Maleki at AIAA SCITECH, Jan. 2024.
- "High-Fidelity Analysis of Synthetic Turbulence Effects on Vertiport Unsteady Flow Characteristics," to be given by Alireza Maleki at AIAA SCITECH, Jan 2025.
- "Navigating the Noise: A CBF Approach for Nonlinear Control with Integral Constraints," to be presented by Idris Seidu at IEEE Conference on Decision and Control, 2024.
- "Effect of Cylinder Wake on the noise of small propeller," to be presented by Jie Hua at AIAA SciTech, Jan 2025.
- "Prediction and Control of Broadband Noise Associated with Advanced Air Mobility-A Review," by Jie Hua and Reda Mankbadi under review at Applied Sciences.

Contents

Technical approach: Tasks

At the core of this research is the development of accurate methods to predict how rotor performance and noise are impacted by the ingestion of large-scale disturbances that exist due to the urban environment. There were five main areas of focus put forward in the proposal each having a number of subtasks

- Urban flow modeling
- Experimental UAM studies
- Computational UAM studies
- Multirotor trim
- Trajectory planning

Grouping the last two under the umbrella of controls, the interaction of the tasks is visualized in Fig. 1. The progress during the first year in each of these research areas are discussed in detail in

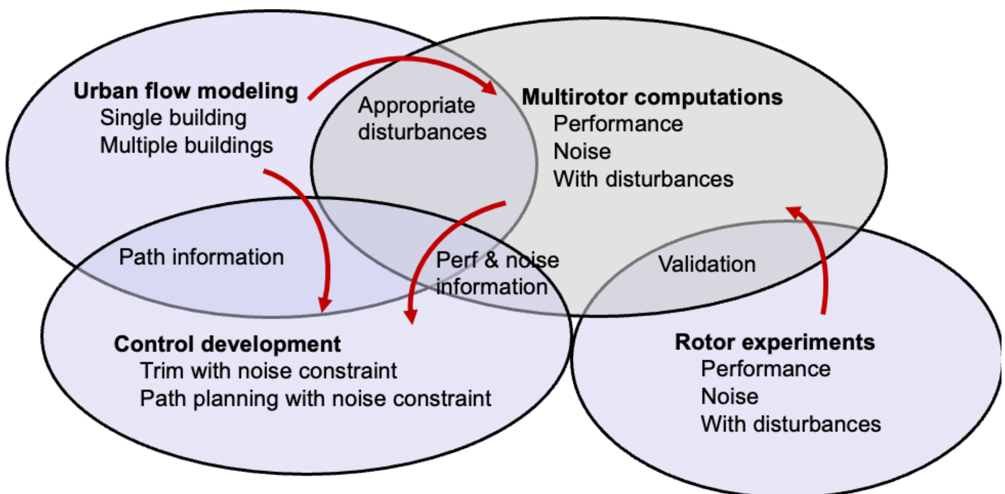

Figure 1: Project diagram with interrelated tasks.

this report. The milestone and gantt charts for each area are reproduced from the original proposal, so that progress can be easily noted.

1 Urban Disturbances

Multirotor vehicles operating in urban settings are expected to take-off and land at vertiports located near buildings and thus will fly through the complex interstitial flows between buildings. As such, understanding better the flow field near buildings and how these change and how they relate to a multirotor vehicle is of interest. Five subtasks provide the framework for our work on urban flow modeling and disturbance characterization. Progress on each is described below.

1.1 Detailed urban modeling

The first task for our urban flow modeling was to verify two existing methods for predicting the flow around buildings. The PALM model is a turbulence-resolving LES model with parameterizations that are optimized for urban applications[1]. For example, individual buildings can be resolved

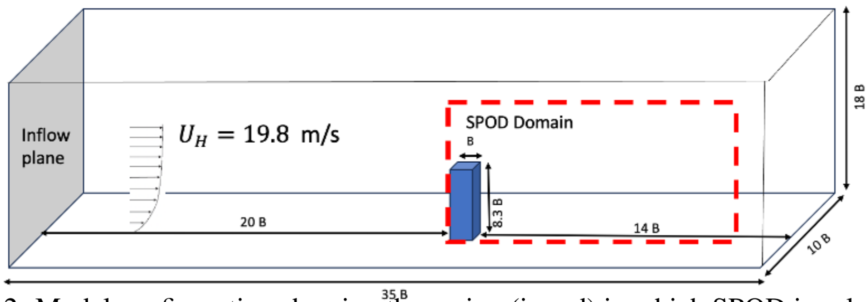

Figure 2: Model configuration showing the region (in red) in which SPOD is calculated.

including overhanging structures like bridges. It has inflow/outflow boundary conditions that can be used to mimic a fully developed, homogeneous boundary layer, which is not affected by buildings downstream. This condition is achieved with the turbulence recycling technique[2]. OpenFOAM also has an LES capability. The pisoFoam incompressible solver was used with the Wall-Adapting Local Eddy viscosity (WALE) subgrid-scale (SGS) model.

A scaled building configuration found in[3] with building aspect ratio of 8.3 was used for the verification. The building width was B= 0.0762 m and the height was H = 0.635 m as shown in Fig. 2. A maximum inflow velocity of 24 m/s is used, which gives a Reynolds number of 110,000. Grid resolution of B/20 is used in all direction. The Inflow/Outflow condition is used in the streamwise direction while a periodic boundary condition is applied in the spanwise direction. No slip wall boundary conditions are used at the ground and building surfaces while a free-slip condition is applied at the domain top. Between the surface (including vertical walls) and the first computational grid-level, a constant flux model with momentum roughness length of B/400 is used. The mean flow and TKE values available in the literature from the experiment were used to validate the methods at the basic level.

Comparison between results from OpenFOAM and PALM highlighted a few important modeling adjustments that were needed in PALM. Normally, the simulation time step is calculated within the model to maintain a Courant number below 0.9. However, it was of interest to have a finer time resolution. Therefore, a time resolution of 5×10^{-5} s was used (Courant less than 0.6) and the velocity field was recorded every 0.001 s.

Usually PALM runs using a recirculating flow method that allows for upstream turbulence to naturally be created in the simulation. This was turned off to enable better comparisons between PALM and OpenFOAM. The differences in the flow around the building with and without an evolved upstream turbulence was tested and is discussed below.

From the OpenFOAM to PALM comparisons, we were able to determine extents to which we can utilize PALM for the urban modeling and what information will easily be accessed from the simulations. More details about the specific disturbance characteristics noted by this work are discussed in subtask 4.

1.2 Urban flow parameter study

Underway now is a parameter study for two common building arrangements in urban areas (aligned and staggered) under different scenarios such as wind speed or direction, stratification, inflow-outflow/periodic boundary conditions and plan area fraction as shown in Fig. 3 and Table 1.

The building height H for these simulations is 10 m with a grid resolution of H/20. The model domain size is 72 H ×36 H ×12 H in the x-, y- and z- direction respectively. PALM's self nesting is

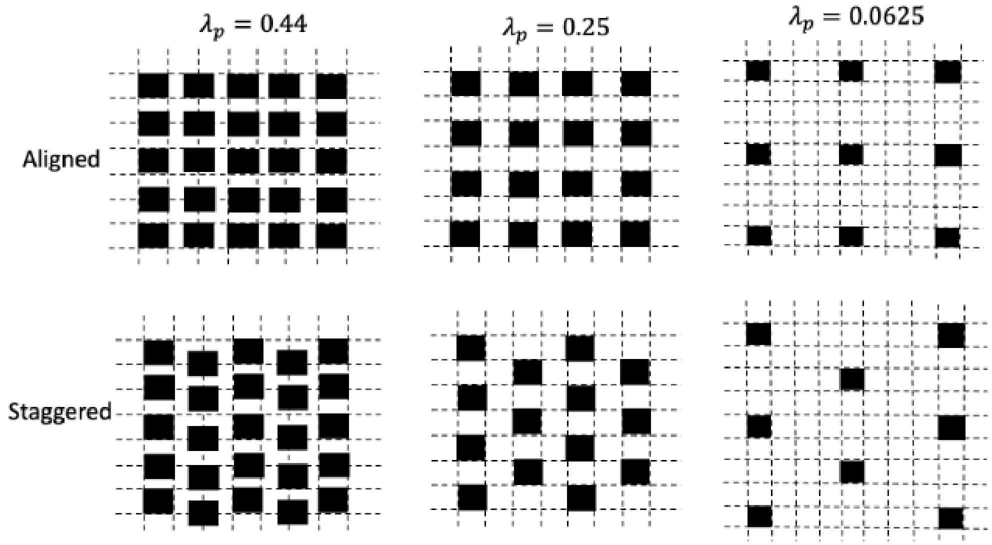

Figure 3: Model configurations for aligned and staggered building arrangement for different plan area fractions.

Table 1: Planned simulation cases and scenarios for the idealized multiple building simulations.

Cases	Orientation	Plan area fraction	Wind speed (m/s)	Wind direction	Stratification
C1	Aligned	0.0625	2	0	Neutral
C2	Aligned	0.257	2	0	Neutral
C3	Aligned	0.44	2	0	Neutral
C4	Staggered	0.0625	2	0	Neutral
C5	Staggered	0.25	2	0	Neutral
C6	Staggered	0.44	2	0	Neutral
C7	Aligned	0.25	15	0	Neutral
C8	Staggered	0.25	15	0	Neutral
C9	Staggered	0.25	15	45	Neutral
C10	Staggered	0.25	15	0	Unstable
C11	Staggered	0.25	15	0	Stable

used to simulate at higher resolution the flow around four buildings within the model domain. The flow fields around and above the buildings are recorded and evaluated for first and second-order statistics (such as mean wind speed, velocity variances, vorticity, TKE and gust or peak factors) and SPOD.

The averaged values of mean velocity and TKE for the two alignments is shown in Fig. 4. The staggered alignment leads to higher values for all of the parameters considered. Fig. 5 shows TKE on an entire plane cutting through the middle of the buildings both horizontally (top) and vertically (bottom). The buildings shown are in the center of the entire periodic grid of buildings. The regions in which the TKE is increased the most are obvious in the figure.

This work is still in progress and will extend to next year.

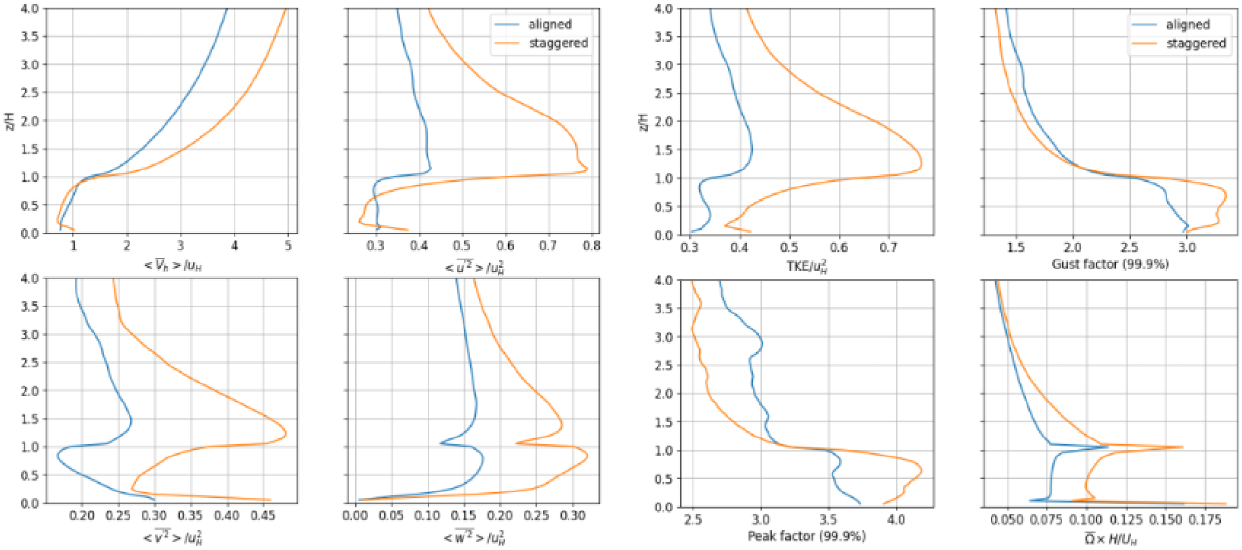

Figure 4: : Profiles of first and second order statistics for cases C2 and C5 (aligned and staggered).

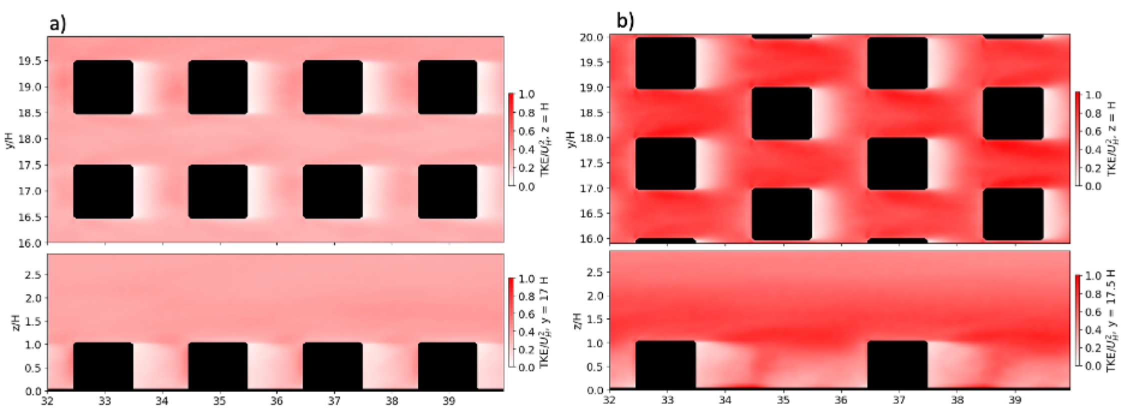

Figure 5: Scaled TKE for horizontal and vertical slice throught the (a) aligned (b) staggered building configurations

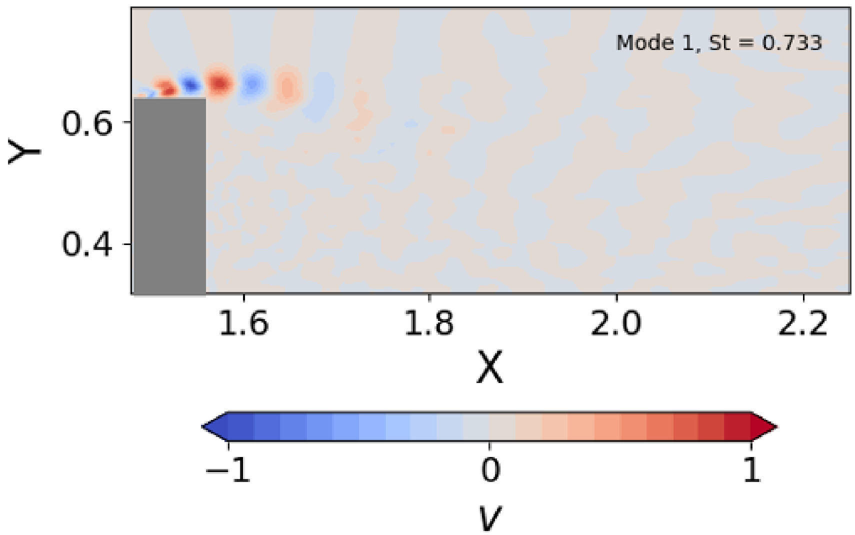

Figure 6: SPOD result at Strouhal number associated with the secondary vortex.

1.3 Realistic urban modeling - planned for Year 3

1.4 Disturbance characterization and modeling

A SPOD (spectral proper orthogonal decomposition) was used with OpenFOAM and PALM to more specifically analyze the unsteady flow field around the building. The plane on which the SPOD was computed is shown in Fig. 2. The flow velocity time history was collected during the final 15 seconds of the flow simulations, out of a total simulation time of 18 seconds, with a recording interval of 0.0005 seconds. For the SPOD analysis, the data was divided into 28 blocks, each containing 1,024 time samples, with a 50% overlap, resulting in a frequency resolution of 0.97 Hz.

The SPOD highlighted various disturbance types in ascending Strouhal number order.

- Base Vortex
- Primary Tip Vortex
- Von Karman Vortex
- Secondary-Tip Vortex

The secondary-tip vortex is depicted in Fig. 6 by visualizing one velocity component from the SPOD. The secondary-tip vortex is of most interest because it exists near the top of the building where a vertiport would be located. The other disturbances are behind the building below it's top surface. While the secondary-tip vortex was a focus of investigation during year 1, the effect of the other disturbance types on downstream buildings is of interest and is being investigated as part of the multibuilding simulations.

The SPOD of the PALM simulation with B/20 cell size resolved the first three structures. The PALM model with 5th order advection scheme could not resolve the secondary tip vortex due to immense numerical energy dissipation at high wavenumbers. PALM with a 2nd order scheme which is less dissipative captured the secondary-tip vortex. To overcome the limitation of the PALM model with 5th order advection scheme, the self-nesting feature of PALM can be used allowing a region above the building to have a much higher grid resolution which then captures the secondary tip vortex.

The predicted Strouhal number for the secondary tip vortex did not match between OpenFOAM and PALM. The Strouhal number associated with the secondary vortex turns out to be dependent

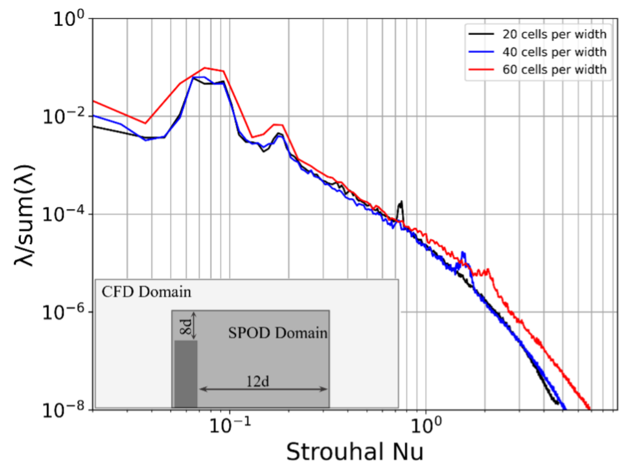

Figure 7: The first mode of the energy spectrum in the mid-span plane of the building.$d = B$ in the insert.

on grid resolution. A separate study to try to understand this dependence better was run. Using OpenFOAM for a case with a lower freestream velocity such that the Reynolds number was 12,000, three levels of grid refinement were considered, with cell sizes of B/20, B/40, and B/60 around the building's rooftop. The total number of cells for each refinement level was 2,400,000, 5,900,000, and 10,350,000, respectively. The results for the first mode are shown in Fig. 7.

Because the SPOD requires a large number of samples to converge, achieving results from OpenFOAM with an even finer grid for a 15 second interval is too time-consuming. To address this, Fast Fourier Transformation (FFT) is used instead to determine the converged value for the secondary-tip vortex shedding frequency. The secondary-tip vortex originates from the fluctuation of the separated boundary layer at the leading edge of the cylinder. To calculate the frequency of this fluctuation, a probe point is placed 0.1B from the front wall and 0.1B above the rooftop of the building.

Fig. 9 presents the FFT results of the wall-normal velocity component at the probe location. The dominant frequency converges at the grids with 80 and 100 cells per width, reaching a value of St = 3.051. We learn from this study that it will not be possible to resolve perfectly this secondary-vortex when doing a full urban simulation. As such, further efforts will be made to relate this disturbance to information readily available in a less refined mesh calculation such as the mean and TKE values.

Looking ahead to how the information from the urban flow modeling will be coupled to the rotor simulations, a few comments can be made. To model the effects of the secondary-tip vortex, a time-harmonic gust will be used. The wave number of the harmonic gust is calculated based on the shedding frequency of the secondary-tip vortex. The amplitude of the harmonic gust can be approximated by the ratio of the wall-normal velocity at the probe point to the inlet velocity. For the case related to Figs. 8 & 9 this value varies between -0.25 and 0.65.

We also considered the impact of atmospheric urban turbulent wind on the flow around the vertiport and its coherent structures, a volumetric source term was introduced upstream of the vertiport within the Navier-Stokes equations. This method imposes a field described by a Fourier spectrum, which includes a superposition of harmonic functions—each term of this superposition corresponds to a single time-harmonic gust. Figure 10 presents the results of this simulation. According to this figure, the turbulence at the inlet does not affect the frequency content of the structures, though it has a reducing impact on the energy of each structure.

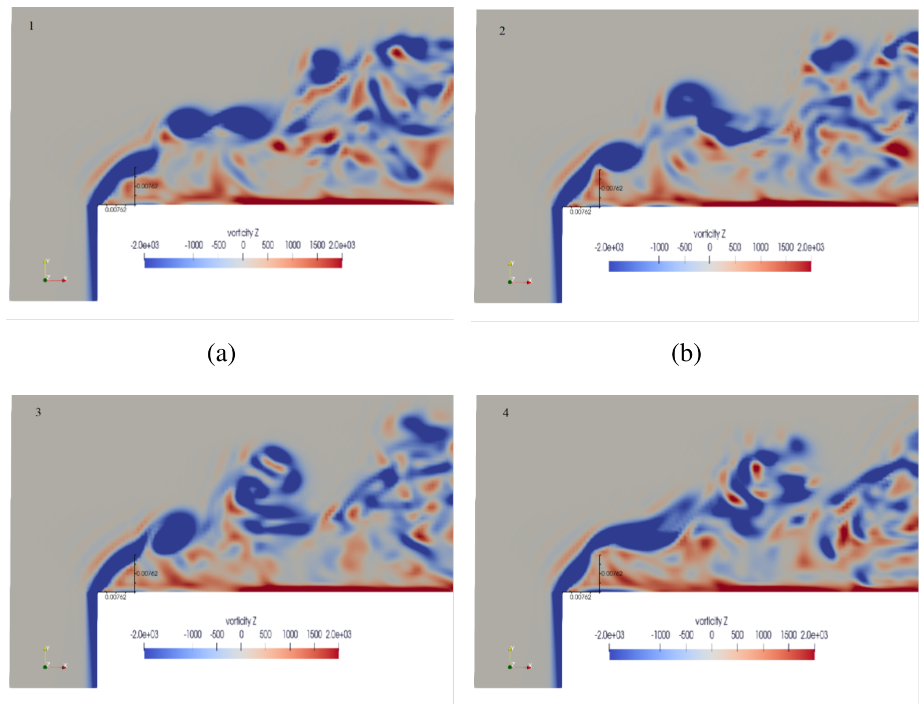

(a) (b)

(c) (d)

Figure 8: Time evolution of the secondary-tip vortex over one period.

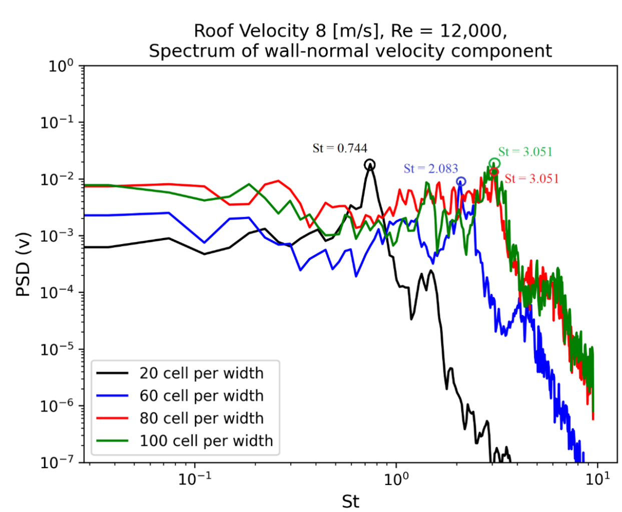

Figure 9: Fourier transform of the wall-normal component of velocity at the probe location.

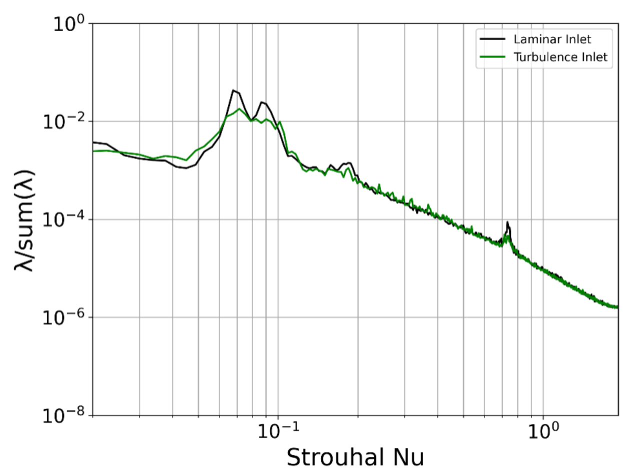

Figure 10: The first mode of the energy spectrum in the mid-span plane of the building in the presence of upstream turbulence.

1.5 Disturbance coupling to rotor simulations

Discussions of how flow variations and disturbances can be introduced into rotorcraft simulations have commenced. The following investigations support this subtask. The asterisk indicates that there is more detail provided in a later section describing the updates on the computational simulations.

- high fidelity rotor simulations with an actual disturbance upstream*
  - OpenFOAM: APC propeller downstream of cylinder
  - Helios : AART case, small propeller downstream of fixed wing
- Successful implementation of method for allowing moving, overlapping grids in OpenFOAM has been tested to enable simulation of moving wing upstream of a rotor like the planned experimental disturbance generator. This is of interest to allow maintaining high quality grid quality for moving component, independent of their respective motion.
- Start of simulation of an advancing Joby prop with time-varying mean flow based on previous flapped airfoil experimental data*
- CHARM - mid-fidelity AART case, mean wake disturbance model; case obtained from CDI and analyzed
- Previous work using injection of synthetic turbulence into a high fidelity simulation reviewed; used in the urban flow modeling but not yet with a moving rotor

The initial results from the implementation of the overset (Chimera) grid method in OpenFOAM show promise. The overset method works with the overSimpleDyMFoam (steady state) and overPimpleDyMFoam (transient) solvers. The movement of the wing is modeled via 6DoF movement, allowing both harmonic or non-harmonic motions that experimental analysis can produce. A NACA 0021 wing-section deflection was simulated using a $k-\omega$SST model with the first wall-normal cell-center height at $\triangle y^+ = 15$. A wall function model (log law) is used. The conditions were set to match those of the previous experiment at VT: $U_\infty = 20$m/s and $Re = 200$k. An angle of attack change from 0 - 20^o in 40 ms is prescribed. The grid is shown in Fig. 11. The x & y-components of the velocity field as a function of time at a position downstream of the wing where the PIV plane was set is shown in Fig. 12. The figures have been stacked at matching non-dimensional times. The amplitude and timing of the unsteady disturbance created by the flapped wing are in relatively good agreement.

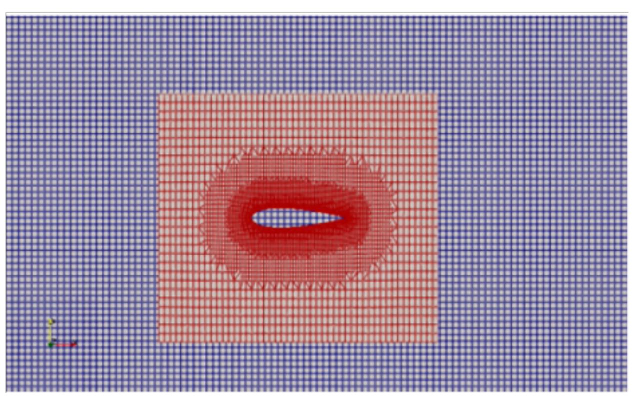

Figure 11: OpenFOAM overset grids containing background mesh (blue) and moving wing mesh (red)

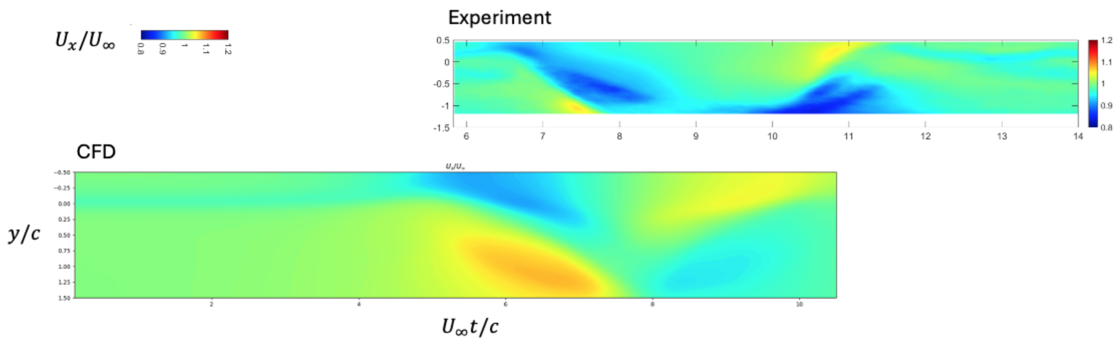

(a) x-component

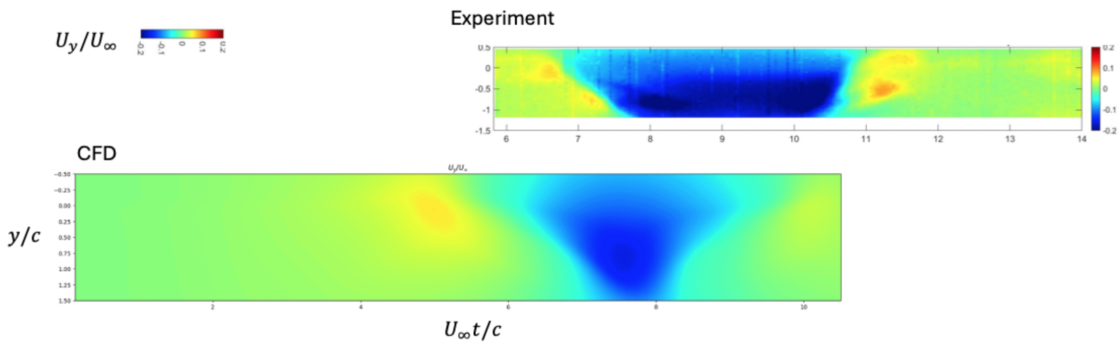

(b) y-component

Figure 12: x & y-components of velocity down stream of flapped wing as function of time.

Table 2: Milestones and Deliverables for Task 1

Milestone/Subtask /TC/Start-End	**Description (Dependency)**	**Exit Criteria**	**Deliverables**
M1.1/Task 1.1 TC 1/ Q1-4	Detailed urban modeling	Validated urban benchmark completed at high resolution	Simplified urban model configuration (grid), test results, documentation
M1.2/Task 1.2 TC 1,3/Q3-8	Urban flow parameter study (M1.1)	Verification of trends based on wind speed and direction; building config.; stratification	Database of urban simulations for different conditions, documentation
M1.3/Task 1.3 TC 1,2,3/Q9-12	Realistic urban modeling (M1.1,2)	Complete Boston based simulation with 0.1m resolution	Boston flow simulation results (grid, output files) Documentation
M1.4/Task 1.4 TC 1 /Q1-12	Disturbance characterization & modeling (M1.1,2;M2.1)	Disturbances from sims and experiment mapped onto canonical disturbances, scaling	Weighted listing of disturbance types and relevant parameters for describing urban flows
M1.5/Task 1.5 TC 1,2,3/ Q2-5	Disturbances coupled to rotor simulations (M1.4;M3.1,2)	Successful demonstration of stable runs	Example response of rotor to canonical disturbances, documentation of coupling methods

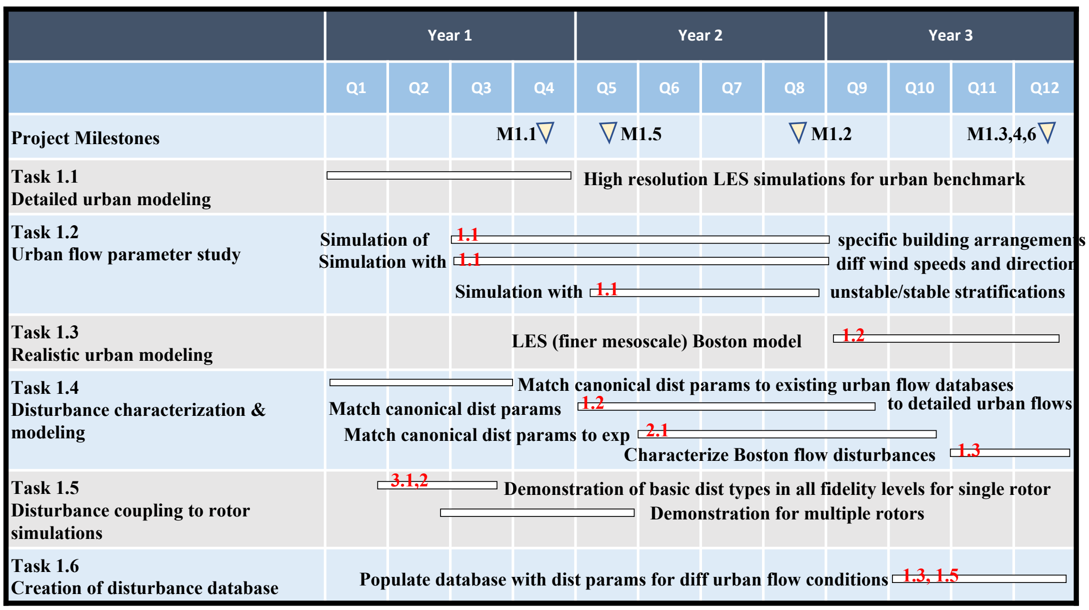

Figure 13: Task 1 schedule. Red indicates required tasks.

2 Experimental UAM studies

Significant progress has been made experimentally in this research program, and these developments are on track with the original timeline of the proposal. In particular, the design and fabrication of a 24” diameter rotor was completed. The aerodynamic and acoustic performance of the rotor was tested at different tilt angles, RPM, and inflow velocities in the Virginia Tech Stability Wind Tunnel. These data will be used for comparison with measurements conducted with a disturbance generator positioned upstream. The design of this disturbance generator is complete and fabrication is nearly complete. Initial wind tunnel tests are planned in the Virginia Tech Anechoic Open-Jet Facility this fall to characterize the wake of the disturbance generator at the planned location of the rotor plane. The following sections detail the results and progress regarding the rotor and disturbance generator. The other tasks in this area are for future years.

2.1 Selection of propeller geometry and baseline experiments

In collaboration with our partner Joby Aviation, we designed and fabricated a 21% scale version of the rotor that flew on their full-scale demonstrator in 2017[4]. This rotor was designed to be variable pitch and tilt. Due to scale constraints, the inner radius of the blade was modified near the blade root to allow the rotor blades to pitch. The pitch is manipulated manually with a calibration plate. Each blade was manufactured individually through an injection molding process by Piranha Propellers using Nyling 6/6 using embedded long carbon fibers (40% by weight) to increase the material strength. The rotor and shafting were dynamically balanced at American Hofmann Corporation to reduce mechanical vibrations during testing. The rotor is powered by a Kollmorgen servomotor (6.95hp) with an optical encoder to relay absolute blade position. For measurement of aerodynamic performance, specifically thrust and torque, this drive system was mounted to a 6-component JR3 load cell. The entire rotor assembly was installed in the Virginia Tech Stability Wind Tunnel on a precision turntable to accurately control tilt. Fig. 14 shows a CAD drawing of the design and a picture of the final installed model.

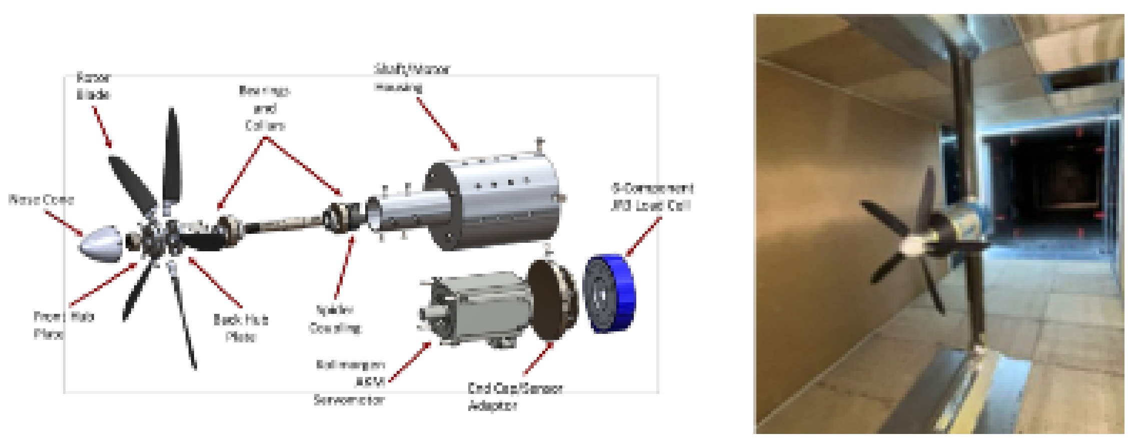

Figure 14: CAD of rotor design and installation of model in test section of the Virginia Tech Stability Wind Tunnel

This new experimental rig was tested in March 2024 considering different rotor tilt angles: 0° (axial), 70°, 80°, and 90° (edgewise). The rotor RPM was varied from 1000 to 4000 and was

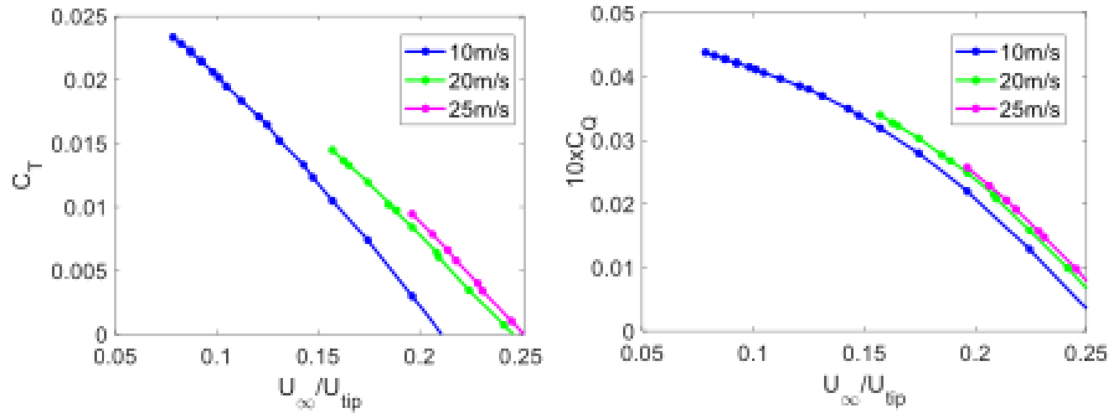

Figure 15: Thrust and torque for 16° pitch condition in axial flight (0° tilt)

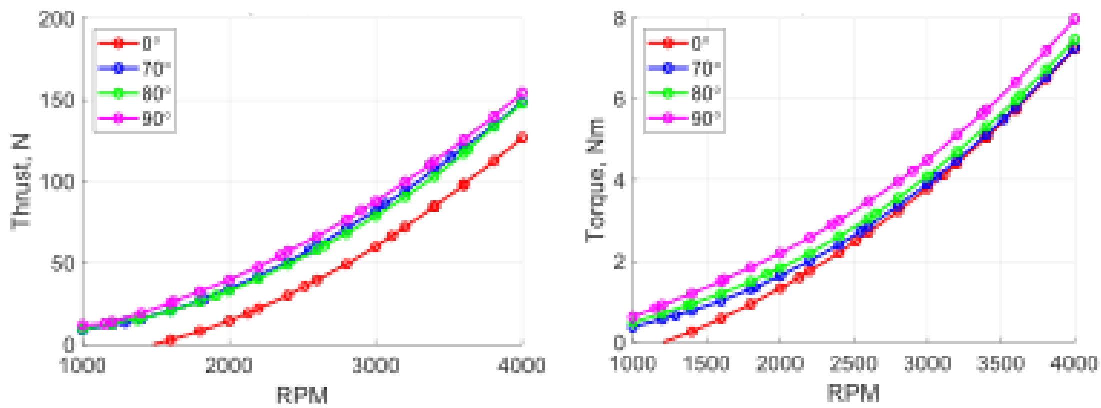

Figure 16: Effect of rotor tilt on thrust and torque, 16° pitch, U_∞ = 10m/s

selected about a condition which matched the full-scale rotor's tip velocity. The inflow velocity was varied between 10 and 25m/s. A hover condition, 0m/s, was examined as well. Three blade pitch angles, measured at 75% radius, were studied: 12°, 16°, and 20°. The 16° condition was selected as the baseline configuration as this is the design pitch at hover for this rotor. A sample of the data collected during this initial test are shown below. The complete analyzed data set will be shared with project collaborators and published on a public website hosted by Virginia Tech. Fig. 15 shows the normalized thrust and torque for the 16° pitch, 0° tilt condition at different inflow velocities. As expected, the thrust and torque decrease with increasing inflow velocity. In addition, the normalized values diverge at low tip velocities suggesting that Reynolds number effects are important at these conditions. The performance data tend to converge at higher tip velocities though. BEMT calculations of thrust (not shown) agree well with these measurements. Although, the torque is underpredicted likely due to effects of mechanical torque which haven't been accounted for in these data.

The effect of rotor tilt on thrust and torque is shown in Fig. 16 for a constant inflow velocity of 10m/s. Tilting the rotor from axial, 0°, to edgewise, 90°, flight increases both the thrust and torque.

The noise produced by the rotor is being evaluated with several different methods. Individual microphone spectra are being analyzed along with beamform maps and directivity maps. Spectra of the rotor noise in axial and edgewise flight for 3806 RPM and 16°pitch at 10m/s are shown in Fig. 17 compared to the background noise levels at a fixed microphone position upstream of the rotor and

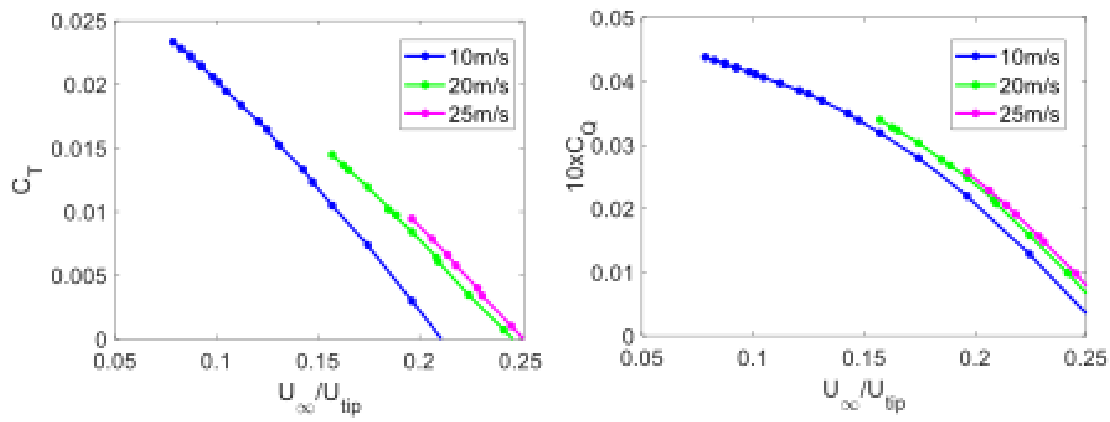

Figure 17: Single mic spectra of rotor noise in axial and edgewise flight compared to the background noise of the facility at U_∞= 10m/s

48.9° off of the centerline axis of the tunnel. At this microphone position, the signal-to-noise ratio above 375Hz is greater than 10dB. As the rotor rotates from axial to edgewise flight, the noise increases at all frequencies as much as 30dB. The blade passage frequency (BPF) is apparent in both spectra but higher harmonics quickly fall off below the broadband noise levels particularly in edgewise flight. These spectra can be evaluated as a function of RPM as well by plotting these spectra as contours covering many operating conditions.

Figs .18 & 19 show contours of the spectra for axial and edgewise flight at an inflow velocity of 10m/s and all RPM. In axial flight, the rotor is very quiet, particularly at low RPM, as there is no inflow turbulence. The source of rotor noise is entirely due to blade self-noise, steady loading, and thickness noise. Thus, the background noise rises above the rotor noise between 250 and 400Hz. The slanted features in the contour at these frequencies are a result of the interpolation scheme which favors phenomenon lying along lines parallel to the BPF and its harmonics. This does not represent background features well which extend as vertical stripes in the contour until they fall below the rotor noise around 3000RPM. At lower RPM, between 1400 and 2500 RPM, broadband self-noise peaks between 5kHz and 12kHz. This has been observed by others including Hersh et al.[5] for rotors operating at low thrust. In edgewise flight, the rotor is louder at all RPM. The BPF is visible but higher harmonics fall below the broadband noise which dominates the spectrum. Although the inflow turbulence is still very low, broadband BWI noise is expected to be a significant component in edgewise flight.

Fig. 20 shows the directivity of the broadband noise integrated between 400 and 20000Hz. The origin of each plot is the center of the rotor disk and pressure levels have been corrected to a radial distance of 1m assuming an inverse square decay with distance. The contours represent ground observer positions. So, in axial flight, the rotor plane is aligned vertically in the contour. For edgewise flight, the rotor is rotated 90° so it is parallel with the plane of the page. There is a minimum in the sound pressure level just ahead of the rotor disk plane in axial flight. As the rotor moves into the edgewise condition, the peak in the broadband noise shifts upstream of the blade disk and is asymmetric. The source is louder on the retreating side of the blade disk in edgewise flight. The broadband noise increases dramatically at all locations compared to the axial condition as well.

Beamform maps identify the source location as perceived at different observer positions. Fig. 21 shows beamform maps produced by different sub-arrays of the 251-channel microphone array for

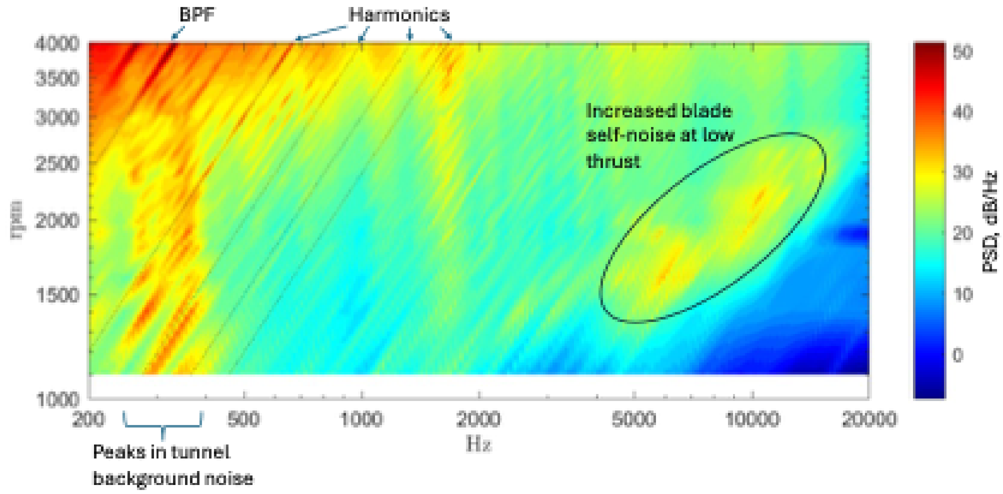

Figure 18: Contour of single mic spectra for 16° pitch, axial flight at U_∞ =10 m/s

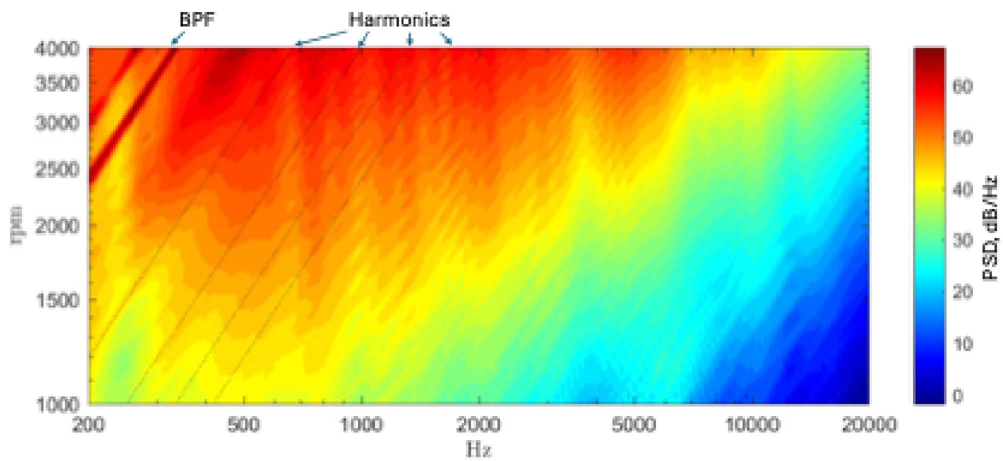

Figure 19: Contour of single mic spectra for 16° pitch, edgewise flight at U_∞ =10 m/s

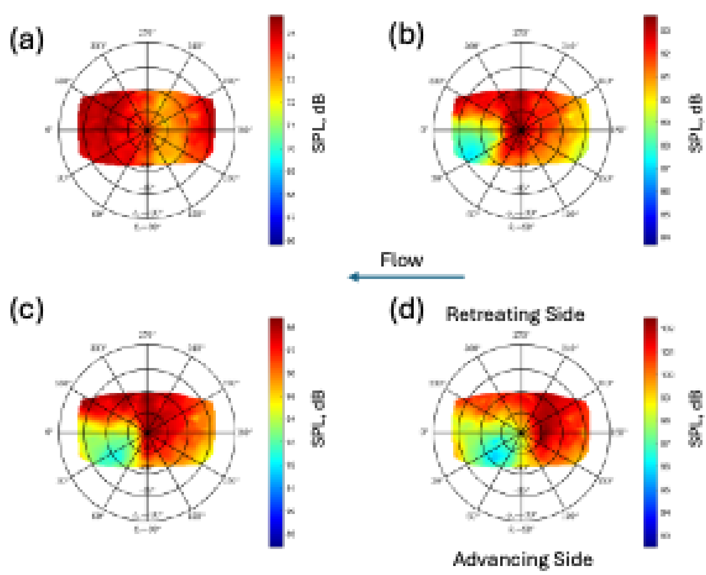

Figure 20: Integrated sound pressure level for all micropohones in the array for (a) axial flight, 0°, (b) 70°, (c) 80°, (d) and edgewise flight, 90°

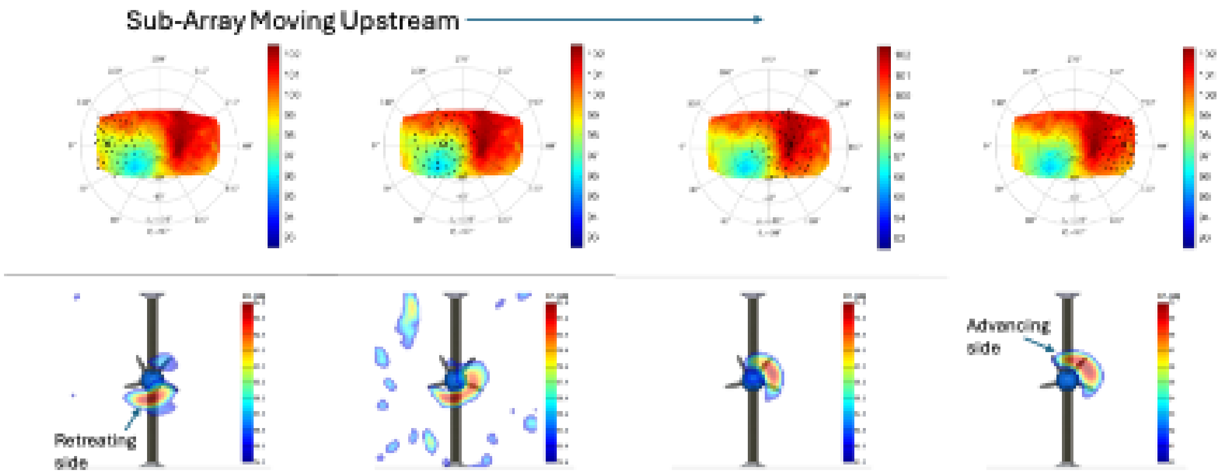

Figure 21: Directivity maps showing the position of the sub-array (black dots) used to produce the beamform maps for a 1/12th octave-band centered at 4kHz

a 1/12th octave-band centered around 4kHz for the rotor in edgewise flight. The rotor plane is parallel to the plane of the microphones. Thus, the array can resolve the source distribution across the rotor disk well. As the observer moves from a position downstream of the rotor to upstream, the perceived source location transitions from the retreating side to the advancing side, respectively. The acoustic data presented in Figures 4 through 8 will be compared to time-dependent results obtained from measurements of the rotor interacting with an unsteady inflow in our next experiment in the Virginia Tech Stability Wind Tunnel. This test is currently planned for Feb.-Mar. 2025.

2.2 Characterization and matching of disturbance generator flow

Design of the disturbance generator is complete, and fabrication is underway. The disturbance is to be produced by a flapping 152mm chord, 1.8m span NACA 0021 airfoil. The device is controlled using two Dunkermotoren servotube linear actuators, one positioned in the floor and the other in the ceiling of the wind tunnel's test section. The actuator control has been tuned to ensure that the actuators trigger simultaneously and stay synchronized during their motion. Fig. 22 shows the CAD of the actuator device installed in the test section upstream of the rotor and a picture of the assembly during benchtop testing in the lab. The streamwise location of the disturbance generator relative to the rotor is still variable and will be based on the results of initial measurements of the disturbance wake. We are currently considering positioning the airfoil two rotor diameters, 1.2m, upstream of the center of the rotor. The actuation rate can be controlled to change both the total timescale as well as the magnitude of the disturbance. It has been designed to flap from 0° to 20° and back in as fast as 40ms. This actuation rate, although rapid, is not fast enough to produce a simple wake consisting of isolated vortices like discussed in Vader et. al.[6] Instead, the wake is expected to be broadband and turbulent. A similar device, 152mm span, was constructed for a previous ONR-sponsored project. Figure 10 shows the wake produced by this airfoil performing a similar flapping maneuver. In this figure, the mean disturbance velocity field and turbulent velocity field are shown separately and are computed from many phase-locked measurements of the actuation. In addition, we have found that the mean velocity disturbance can be closely represented by an unsteady potential flow calculation like shown in Fig. 23(c). This enables quick estimation of the wake dynamics that can be used for simplified models of the rotor wake interaction which can also help in the design of the

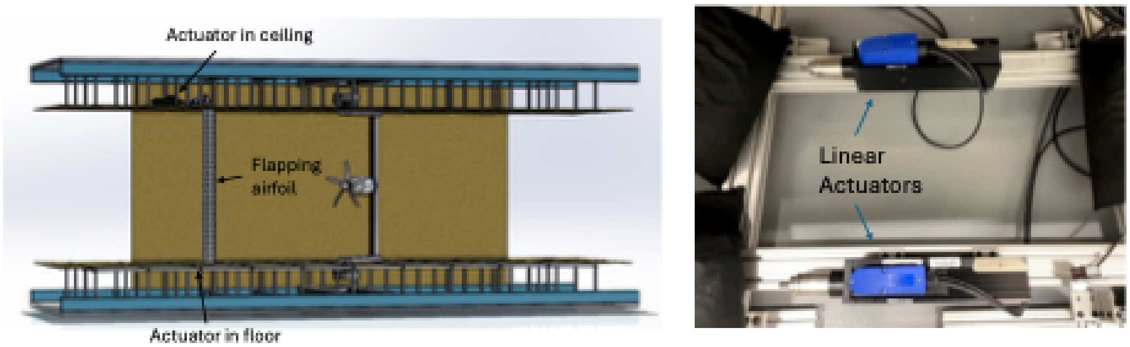

Figure 22: CAD of flapping airfoil installed in the Virginia Tech Stability Wind Tunnel and picture of actuators during bench testing

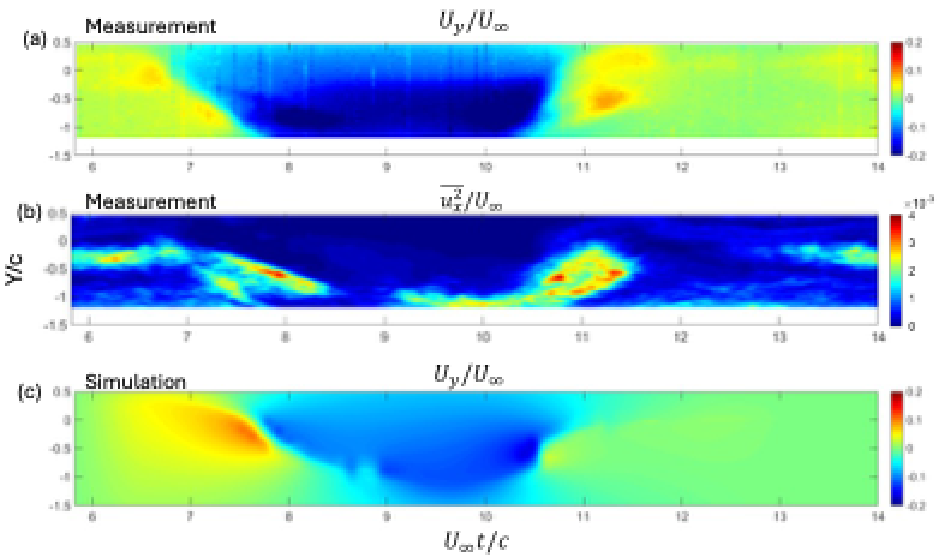

Figure 23: Turbulent wake produced by a flapping airfoil, measurements (a)-(b) compared to mean flow simulation (c)

experimental test matrix.

2.3 SWT measurements of single rotors subject to disturbances - Planned for Year 2

The next milestone for this portion of the project will be the characterization of disturbances produced by different actuation profiles. We are on track to complete this in Q5 this fall. The experiment planned in Q6 in the Virginia Tech Stability Wind Tunnel will investigate the interaction between the rotor and these disturbances.

Table 3: Milestones and Deliverables for Task 2

Milestone/Subtask /TC/Start-End	**Description (Dependency)**	**Exit Criteria**	**Deliverables**
M2.1/Task 2.1 TC 1,3/ Q1-4	Characterization & matching of disturbance generator flow (M1.4;M3.1,2,3;M4.1)	Aerodynamic and acoustic measurements of disturbances	Time-resolved data of disturbance for comparison with urban flow simulations and computational models
M2.2/Task 2.2 TC 1,2/Q1-2	Selection of UAM rotor geometry (M3.1,2,3;M4.1)	Agreement on rotor configurations by proposal team and NASA POC	Detailed propeller characteristics necessary for fabrication
M2.3/Task 2.3 TC 1/ Q2-6	SWT perf. and noise measurements of single rotors subject to disturbances (M1.4;M3.1,2)	Acquisition and analysis of perf and noise data for single rotor configurations subject to a family of disturbances	Thrust and torque. Unsteady velocity near the rotor showing interaction with disturbances and noise measurements at multiple observer locations.
M2.4/Task 2.4 TC 2,3/Q3-9	SWT perf and noise measurement of multirotor with diff trim conditions (M4.1)	Acquisition and analysis of perf and noise data for multirotor configurations at diff trim settings	Acoustic measurements and individual rotor perf data as well as unsteady velocity into downstream rotors
M2.5/Task 2.5 TC 1,2/Q8-10	SWT perf and noise measurement of multirotor subject to disturbances (M3.3;M4.1,2)	Acquisition and analysis of perf and noise data for multirotor configurations interacting with a family of disturbances	Unsteady velocity measurements of disturbances as they interact with the rotors and their effect on the rotor wakes as well as noise at multiple observer locations. Individual rotor perf.

2.4 SWT measurements of multirotor configurations with different trim conditions- Planned for Year 3

2.5 SWT measurements of multirotor vehicles subject to disturbances - Planned for Year 3

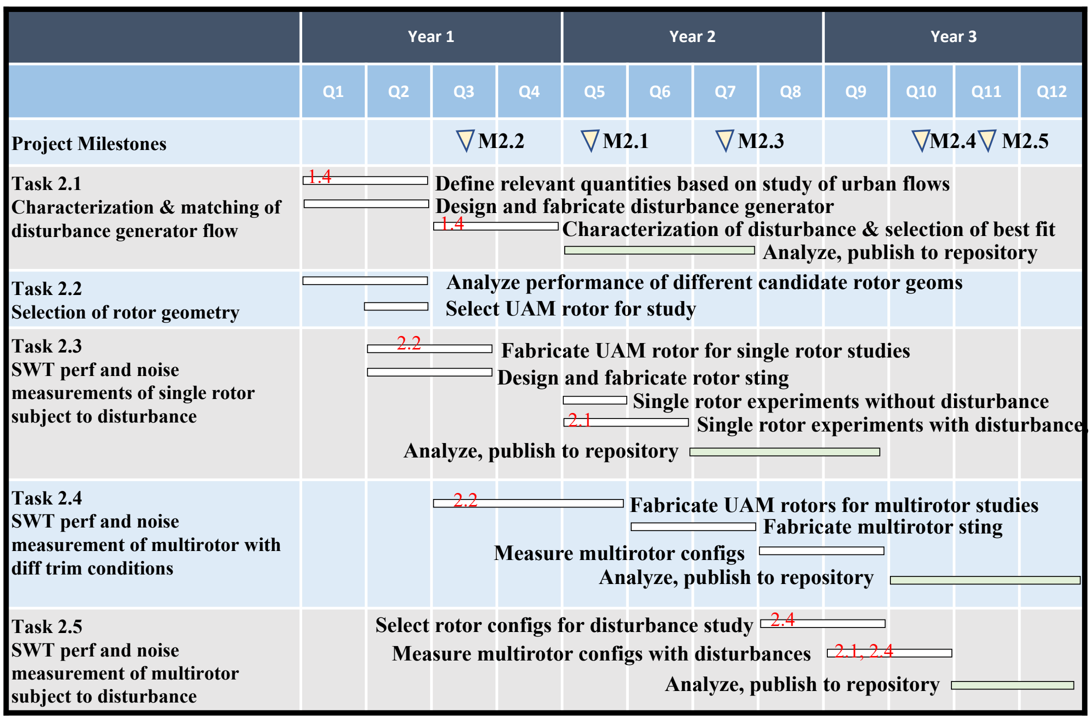

Figure 24: Task 2 schedule. Milestones set at completion of experimental campaigns. Red indicates required tasks.

3 Computational UAM studies

A main focus of this work is accurate computational prediction of multirotor performance and noise. During the first year, much effort was spent learning, verifying, and validating relevant computational tools. There were three main subtasks proposed originally. The implementation of the subtasks overlapped during the first year. The overlap will be pointed out when appropriate.

3.1 Validation of high fidelity simulations

Two high fidelity codes are being applied in this work: (1) OpenFOAM and (2) Helios with near-body solver Overflow. Both couple to a Ffowcs-Williams and Hawkings solver. Currently, libAcoustics[7] is being used with OpenFOAM, while Helios is being coupled to PSU-WOPWOP.

The Helios code was previously validated for small prop (Tmotor) and small quadrotor (SUI Endurance) performance and noise[8]. Therefore, focus was placed on its ability to model the AART case of a small rotor behind a fixed wing. This effort leveraged work already being done by the Army DEVCOM Aviation and Missile Center. Different turbulence and transition models were tested to examine their impact on performance and acoustics. For example, Fig. 25 shows surface pressure differences between simulations using the fully turbulent Spalart-Allmaras (SA) turbulence model and the Spalart-Allmaras turbulence model with Coder's Amplification Factor Transport model for laminar to turbulent transition (SA-AFT). The SA-AFT model produced higher total thrust but a lower impulse from wing-blade interaction resulting in overall lower acoustics. A mesh study is being carried out to analyze these differences further.

This case was also used to study in depth the use of impermeable vs permeable FWH surface for determining the tonal noise. First, the influence of the selection of the permeable surface was tested. Open end-cap permeable surfaces with different extents in the wake of the propeller were used to compute the noise at the experimental microphone locations. A side view of the surfaces is shown in Fig. 26 as well as the summation of the first 10 harmonics at the microphones with increasing downstream surface extent. Unsurprisingly, the downstream microphones, 7 and 13, are the most affected by changing the extent of the sides of the permeable surface. It was also of interest to consider the effect of end cap averaging. Fig. 27 shows the acoustic hemisphere from upstream to downstream around the wing and propeller computed using an open end cap and by averaging the pressure at the microphone from closed surfaces ending at the 7th through 10th end caps. The difference between the two methods is very small indicating that the open end cap method may be the most efficient method. However, this is still under consideration.

Finally, the comparison between the permeable and impermeable FHW was considered. The open ended longest surface was used for the permeable surface. Shown in Figs. 28 & 29 are the results at each of the microphones. The impermeable and permeable do not match perfectly, but there is no specific trend for where or when they do match. The largest disagreements are between the computed results and the experimental results. It is surmised that the experiments include the influence of the microphone stands and other physical objects in the flow. Microphones 7 and 13 are most affected by this.

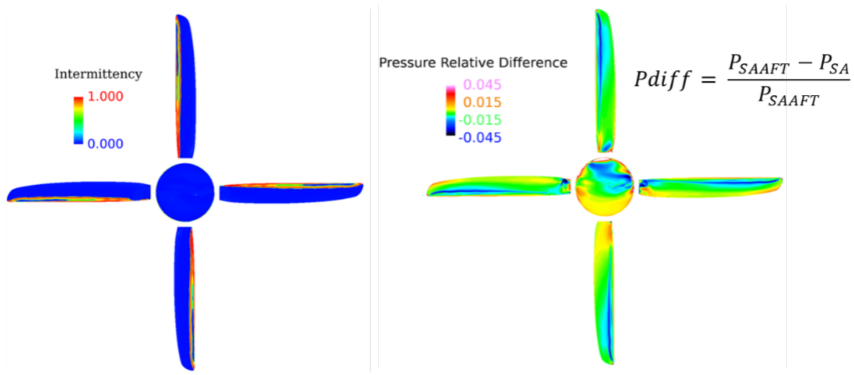

(a) Upper surface

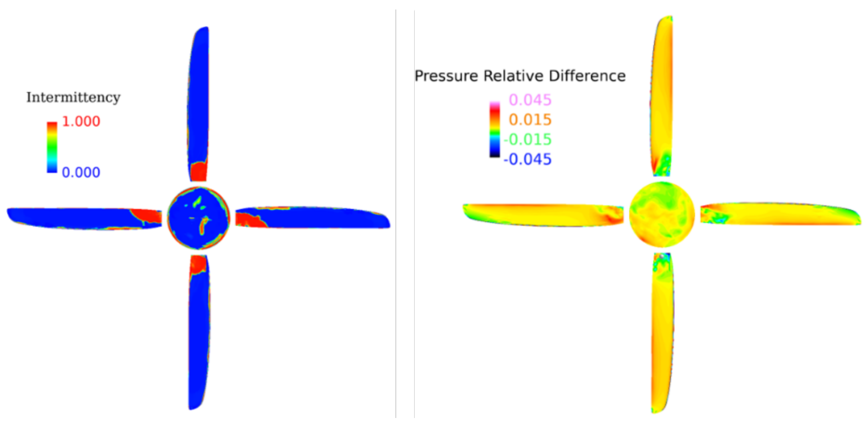

(b) Lower surface

Figure 25: Intermittency and pressure differences on the AART propeller with and without laminar to turbulent transition model.

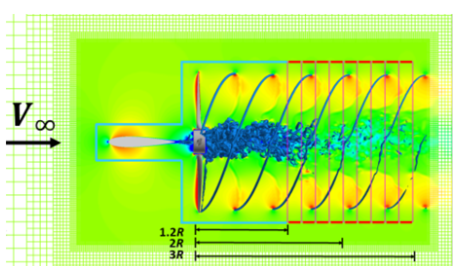

(a)

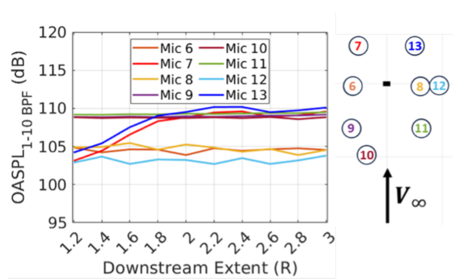

(b)

Figure 26: FWH permeable surfaces with different extents and the sound computed at different microphones using the different surfaces.

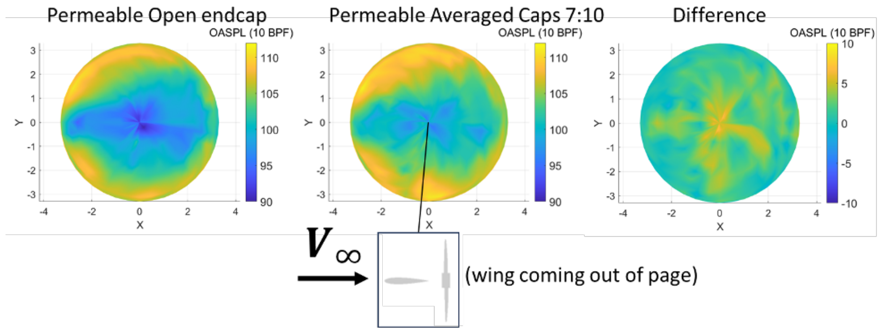

Figure 27: FWH permeable surfaces with no end cap and with end cap averaging.

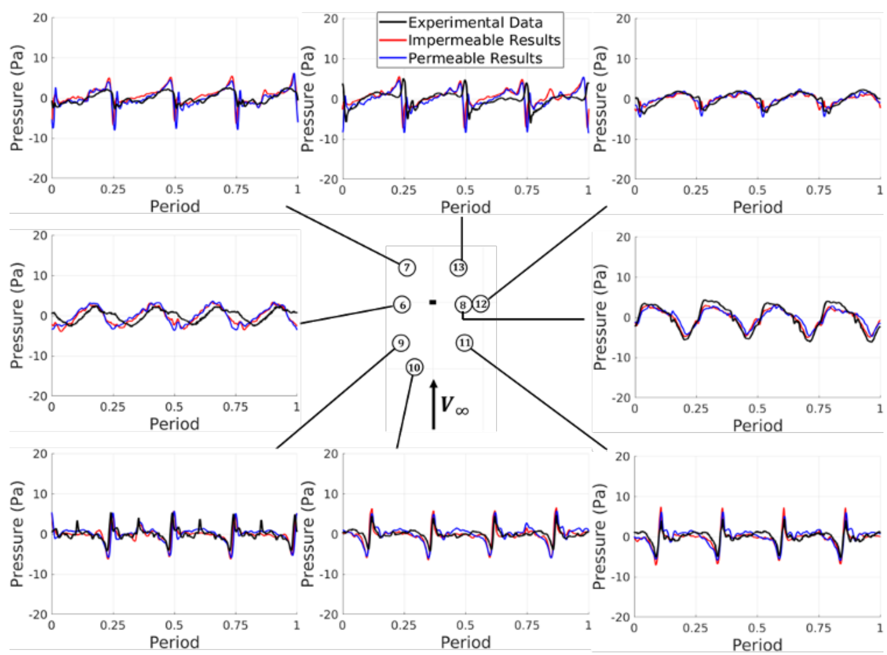

(a)

Figure 28: Pressure vs time at microphones. AART.

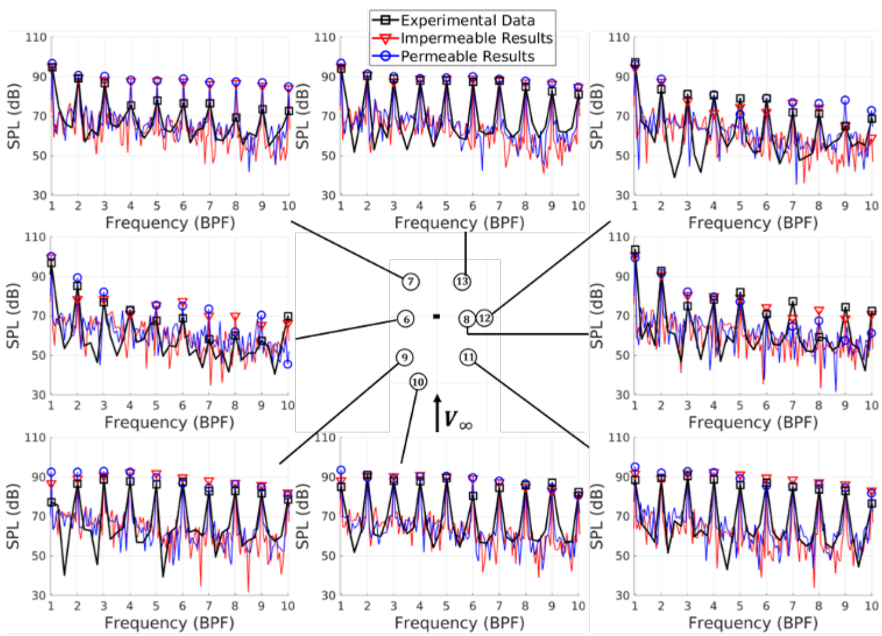

(a)

Figure 29: FFT of pressure at micorphones. First 10 harmonics. AART.

A different propeller with upstream disturbance case was chosen for the OpenFOAM validation work. Yauwenas et al.[9] had conducted an experimental test for the cylinder wake effect on the propeller noise. In their study, the APC 12x6E propeller (12 in. diameter and 6 in. pitch) was used, but manufactured by a third-party. For the present study, a Computer-Aided Design (CAD) model was created based on the airfoil, chord and twist distributions provided on the APC website[10].

Simulations of the rotor were completed for 7000 PRM at hover and then with and without the cylinder at 9000 RPM with an inflow perpendicular to the rotor plane of 20 m/s providing an advance ratio of 0.4374. Comparison of the performance predictions with the experimental data show large disagreement. For the hover case, the experimental coefficient of thrust (prop based) was 0.06 while the computations give 0.08. For the advancing case the experimental C_T (both with and without the cylinder) was 0.0143 while the computed predictions were on the order of 0.045. It is assumed the disagreement stems from geometry differences. In an attempt to validate the computations, additional experimental results for the 12x6E were sought. Two experiments were found in the literature. The first had results for a 6000 RPM hover case and an advance ratio case of 0.43[11]. The second had results for a 7000 RPM hover case and a 9000 RPM advance ratio of 0.43 case[12]. A summary of the results is given in Table 4.

Table 4: C_T for the APC 12 X 6E.

RPM	Flow Speed (m/s)	Computational	Yauwenas et al.	Dantsker et al.	Czyz et al.
6000	0	-	-	0.1078	-
7000	0	0.0808	0.061	-	0.080
9000	20	0.0456	0.0143	0.046	0.0463

There is clearly large disagreement between the Yauwenas et al. experiment and all of the other reported values. This means that the experiment cannot really be trusted which is unfortunate because it was selected due to the fact that noise measurements were made in addition to the performance measurements.

Still, some investigation into the noise calculation was undertaken and the behavior of the noise model was analyzed. A comparison between the permeable and impermeable FWH was initiated for the propeller downstream of the cylinder. Four different permeable surfaces were considered. The main difference was how the cylinder was included within the surface as shown in Fig. 30. The acoustics were processed with and without the permeable surface end cap for each of the surfaces and are shown in Fig. 31. (In the legend, Both refers to with end cap and Top refers to without end cap.) The acoustic prediction turned out to be highly dependent on the choice of permeable surface. The experimental noise results are shown but because the experimental data cannot be trusted, it is not possible to determine which surface provides the most accurate moise predictions.

An attempt to understand the differences in the acoustic predictions based on the differences in the permeable surfaces was made. For surfaces (a) and (d) at low frequency, when one doesn't include the end cap, there is a higher broadband level which indicates that some of the acoustic energy traversing the end cap is missing. This is expected. It is a bit surprising though that when the end cap is used more spurious noise due to the passing of the wakes doesn't appear.

The following outcomes also do not follow intuition:

- Surface (a) has the wake of the cylinder crossing its top cap. Surface (b) has the wake of the cylinder crossing an end cap of the upper portion of the surface. However, the with

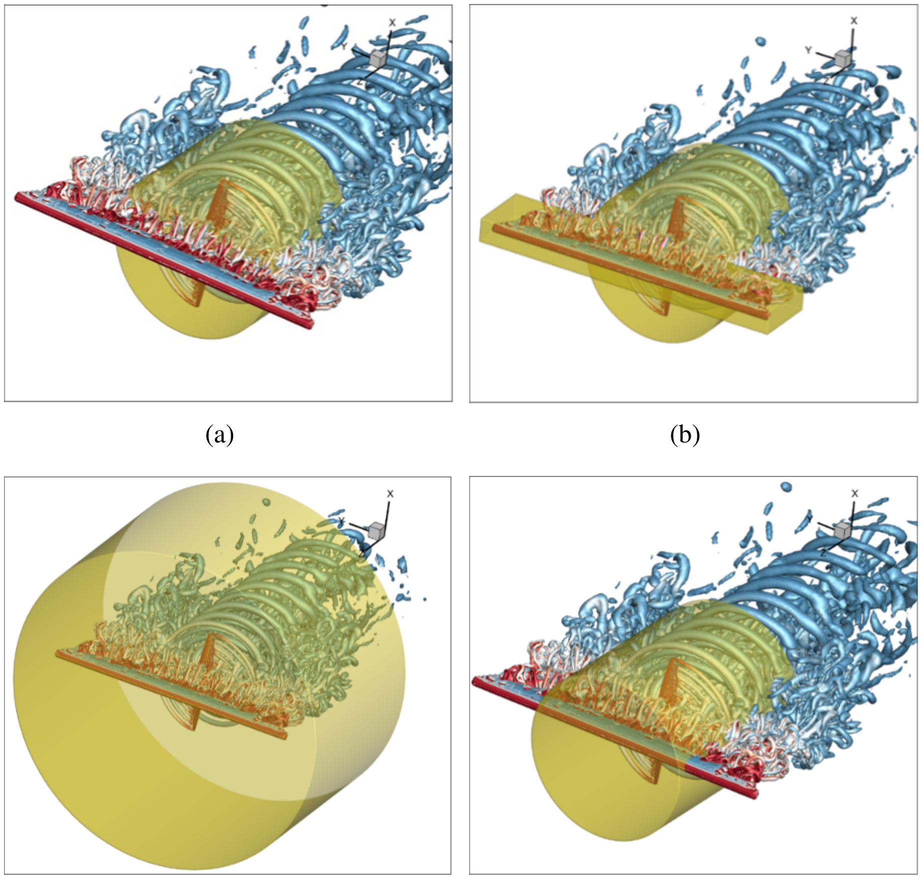

(a) (b)

(c) (d)

Figure 30: FWH control surfaces considered.

and with-out end cap results for surface (b) show very minimal difference while the overall broadband for (b) vs (a) is extremely different. The mismatch in these two outcomes doesn't make sense. If the wake is not strong enough to influence the top cap of (a) then it should not make such a difference from the end cap of (b).

- The tones are much higher for surface (c). This surface is farther away (one would think the pressure would dissipate the farther the surface is from the rotor) and fully encompasses the cylinder. This implies that something about the edges of the cylinder or the edges of its wake are very noisy at the tone of the rotor. It also doesn't match well when compared to surface (d) unless it is the outer part of the cylinder wake that is creating noise at the tone of the rotor.
- The permeable result for surface (d) is compared to the impermeable result in the next figure. The high tonal values from the impermeable surface indicate that the permeable surface method is suffering from dissipation of the pressure waves. A reasonable outcome that is captured is that the broadband content captured with the impermeable would be lower than that found with the permeable.

Joby geometry

As part of this project, it is of interest to model the Joby vehicle. In year one, we began with modeling a single propeller. The experimental data acquired at VT for the scaled Joby prop is being used to validate these computations. The CAD from the VT experiment was used as the base

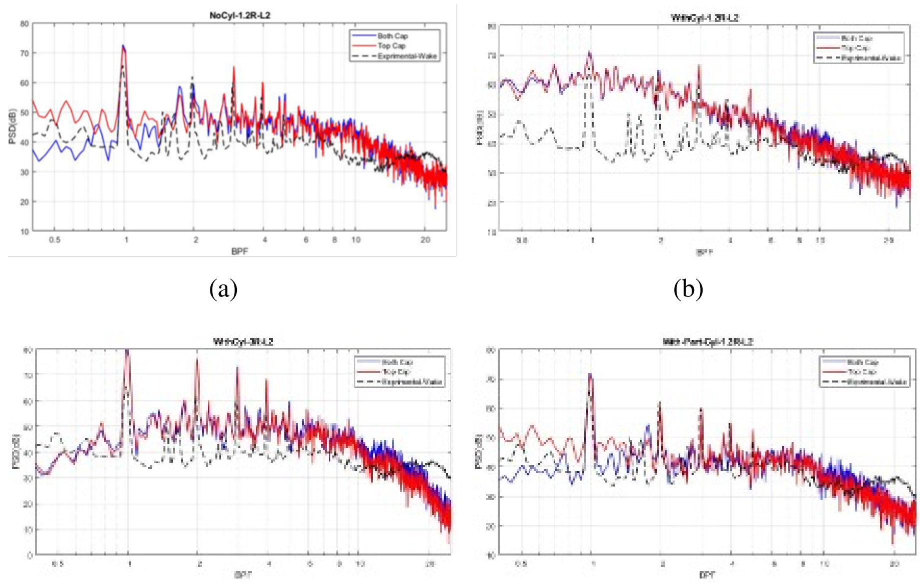

(a) (b)

(c) (d)

Figure 31: Power spectral density of top-capped and both-capped control surfaces.

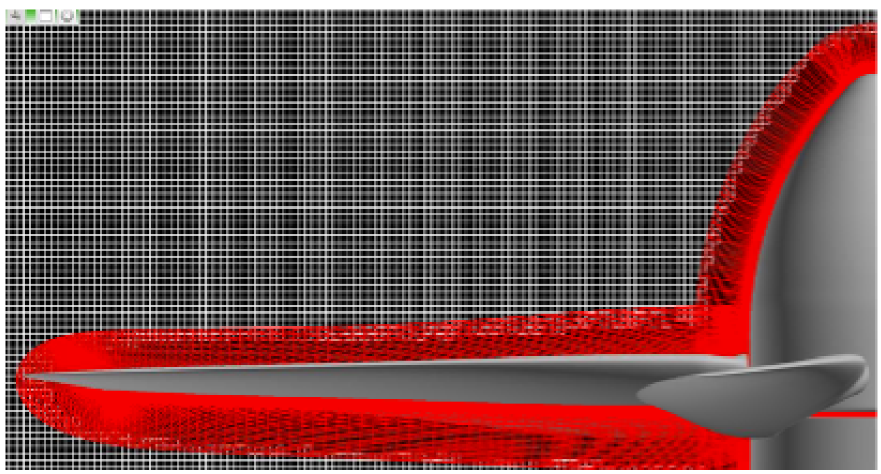

(a)

Figure 32: Grid used for Joby prop with Helios.

geometry and initial simulations have been run in both OpenFOAM and Helios. The propeller has been modeled in configurations with and without the fairing used in the experiment.

A structured near-body was created for NASA's OVERFLOW CFD solver which is supported as a 3rd-party solver in Helios. OVERFLOW requires a structured (cartesian) mesh to enable a 5th-order-accurate central finite difference spatial scheme. This provides higher accuracy than other solvers in Helios, and this solver been found to produce accurate results for other drone-style propeller applications. OVERFLOW meshes of the blade and hub can be seen below in Fig. 32 in red. Helios supports multi-solver overset meshing – the surrounding gray cells are generated by Helios's SAMCART cartesian grid generator and solver.

One operating point has been the focus of the initial simulations: hover at RPM 4000; blade pitch 16 deg at the 75% location. A timestep equivalent to a quarter degree of propeller rotation was

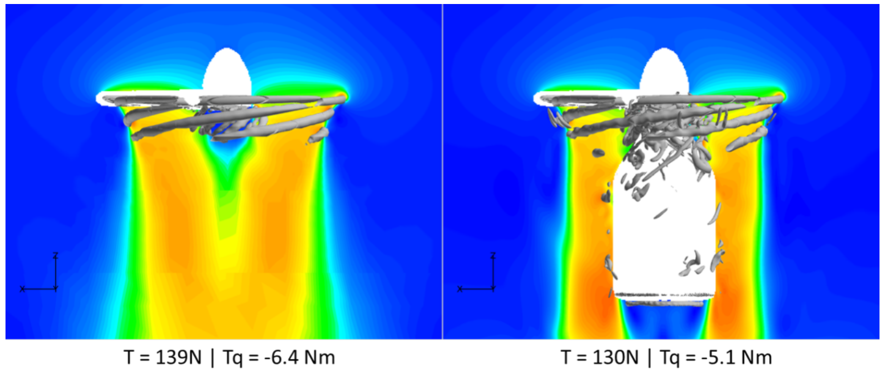

(a)

Figure 33: Results of Helios simulation of Joby propeller with and without fairing.

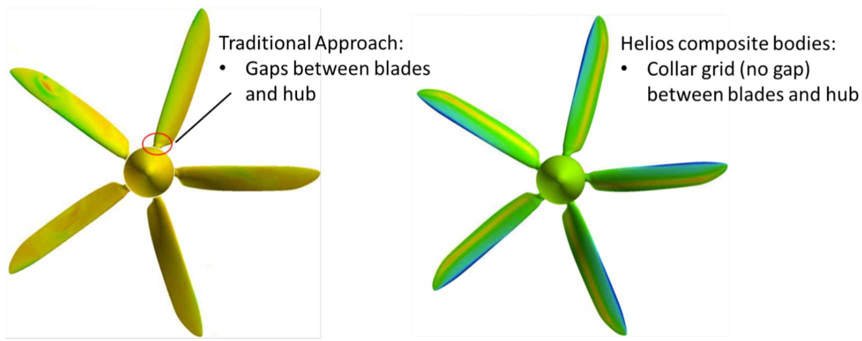

(a)

Figure 34: Different models for the Joby for use in Helios: with and without collar.

used in Helios. The pressure field and Q criterion are visualized for the cases with and without the fairing in Fig. 33. The presence of the fairing resulted in a 6.5% decrease in thrust and appeared to increase BVI. The large difference isn't unexpected, however, the simulation of the propeller without the fairing gives a value of thrust much closer to the experimental value.

Helios's domain connectivity module also allows for the implementation of "composite bodies," or bodies made up of separate grids joined by oversetting a "collar grid" that overlaps the bodies, demonstrated in Fig. 34. A successful composite body mesh system was created for the VT-Joby propeller. Average thrust only changed by about 1%, but the change in root vortex behavior could be important for acoustics. Unfortunately, computational time increased by about 100% from the additional domain connectivity required to make the composite bodies system work.

The grid for the Joby prop developed for OpenFOAM is shown in Fig. 35. The performance values vs time are shown in Fig. 36. The values as they compare to the experimental and Helios results are given in Table 5.

This sets a foundation for further studies of the Joby propeller and vehicle in year two.

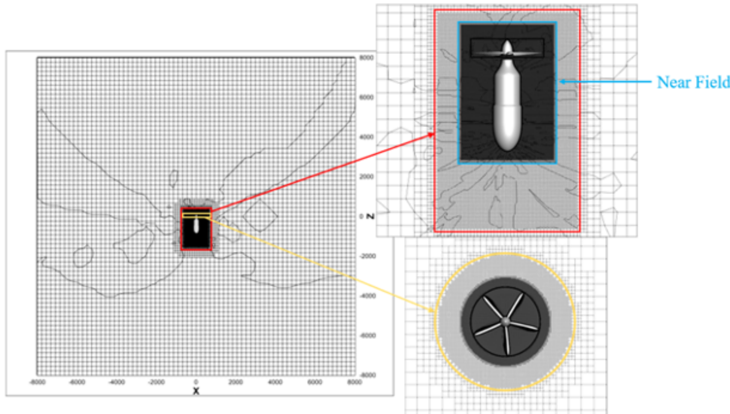

Figure 35: Joby grid for OpenFOAM with fairing.

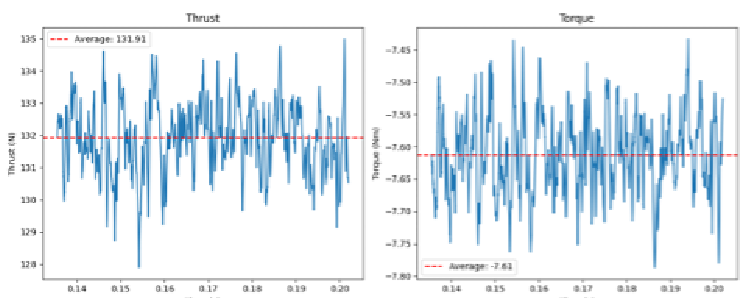

Figure 36: Joby thrust and torque for 5 revs, OpenFOAM, .

Table 5: Joby results

Method		Ave Thrust (N)	Ave Torque (Nm)
OpenFOAM	With Fairing	131.91	-7.61
	No Fairing	130.22	-7.424
Helios	With Fairing	130	-5.1
	No Fairing	139	-6.4
Experimental		138.39	-7.45

3.2 Verification and validation of mid and low fidelity simulations

We have developed methods for effectively using XROTOR for basic prop calculations. And we have a method for performing connected acoustic calculations. This requires us to create a thickness file that is representative of the geometry and put it into the proper WOPWOP format. This became a bit of a diversion as we attempted to develop a good APC thickness file as the geometry information provided by APC is not easily used to identically create an accurate geometry. We leveraged a CAD file that was obtained from APC years ago to test our understanding of their geometry information. We have been able to create an 8x5 Prop that is very close to APC's CAD of this prop. Fig. 37 shows the recreation.

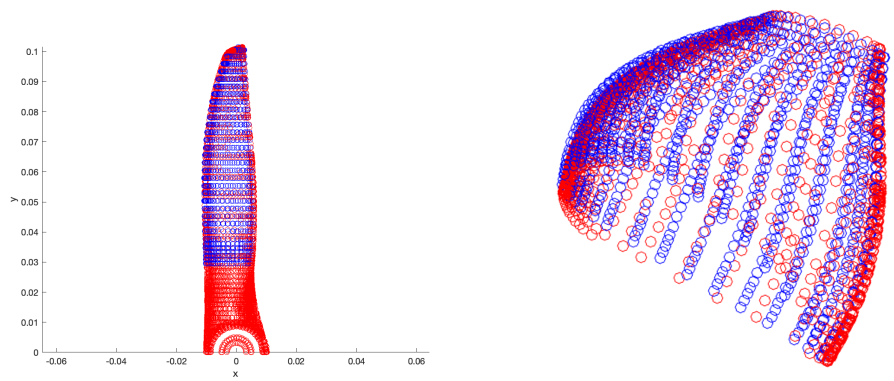

(a) (b)

Figure 37: Recreation of the APC 8x5 prop from the APC geometry information. Compared to CAD obtained from APC.

The entire Xrotor-WOPWOP simulation process was helpful when first analyzing the APC rotors and it is a helpful teaching tool for new students. It is a good tool for getting basic single rotor trends. We utilized the wrappers developed for Xrotor and WOPWOP for the outreach workshop. Xrotor however is not built to handle edgewise flight from what we can ascertain. We have used it only for hover and advancing conditions. Basic phenomenon have been verified such as the effect of two rotors operating in close proximity with similar and different phases.

CHARM has been utilized more fully as it allows for edgewise flight. CDI has been quite helpful and have looked over our simulations and provided feedback on best practices for running the small props. The 9x4 APC prop provided a basis for much of our work and Fig. 38 shows results of many attempts. (XROTOR gave reasonable results for this rotor which was partly why it was selected as the test case.) The legend describes our runs. Our original attempts used the openVSP to CHARM methodology but it ended with a nonrepresentative geometry and gave results that were quite off from the experimental (green only at larger J) and the APC basic BET (cyan). However, we were able to visualize the impact of changing from the included 0012 airfoil table to the ClarkY airfoil table. We even tested a low Reynolds Number Tmotor airfoil table, just to see how it would work. We were also able to test the effect of the number of turns (NREV). After some time, we created our own geometry information without OpenVSP. These geometries gave results that were much more in line with the experimental. The additional legend in larger print was added by Dan Wachspress from CDI. He adjusted the geometry and run files slightly and tested a few options. His

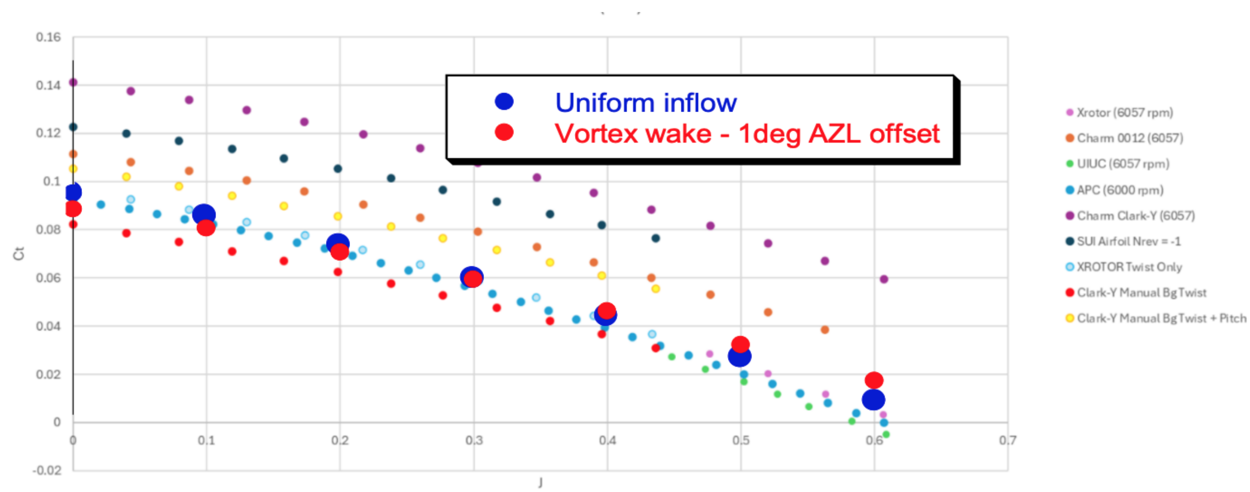

(a)

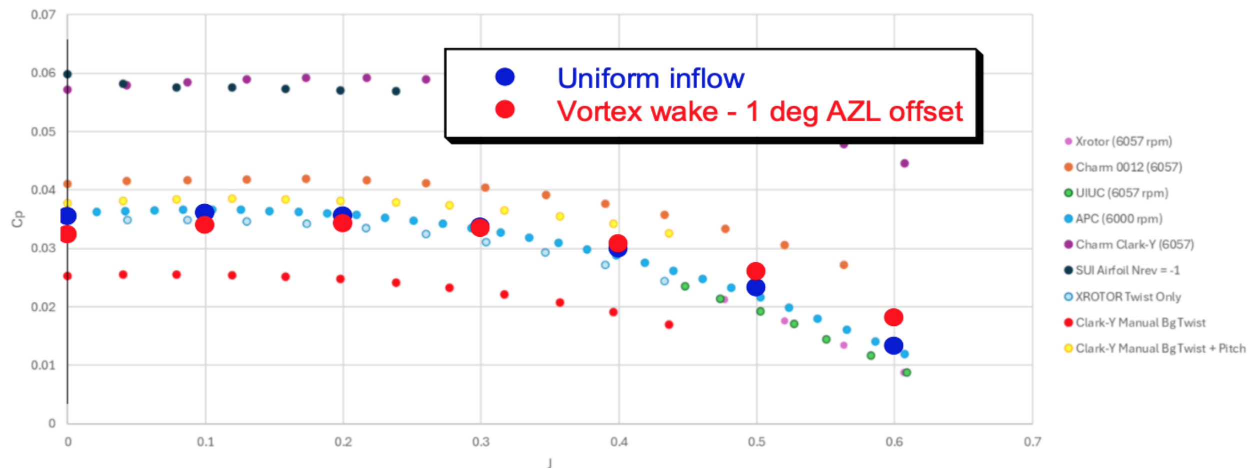

(b)

Figure 38: CHARM performance results for the APC 9x4 propeller.

run was completed using a low Reynolds number ClarkY airfoil table. He believes the discrepancy that remains is most likely fixable with a better airfoil table.

What was learned from the APC modeling gave us confidence to move to the SUI Endurance prop (Tmotor) and vehicle. There are experimental results from NASA for this vehicle and its propeller and there are many CFD results from a past BU thesis. The single prop had been analyzed by CDI previously and we have recovered their results. All of the results have been overlayed onto figures from Austin Thai's thesis. The CHARM results are shown as purple dots and red X's. The hover results for C_T are shown in Fig. 39 The results for the single propeller in a forward flight condition of 20 ft/s at different tilts are given in Fig. 40. The moments do not align well. The results have been developed using a low Reynolds number airfoil table for the Tmotor propeller supplied by CDI. CDI notes that they have no idea why the moments are not matching here.

The Tmotor prop was then used in some full vehicle simulations. The validation results have been pulled from the NASA TM by Russel et al.[13] The hover force results compare fairly well as shown in Fig. 41. The highest RPM cases does not agree as well. CHARM can use Reynolds number correction. This was tested and it did not change the results in any noticable way. The

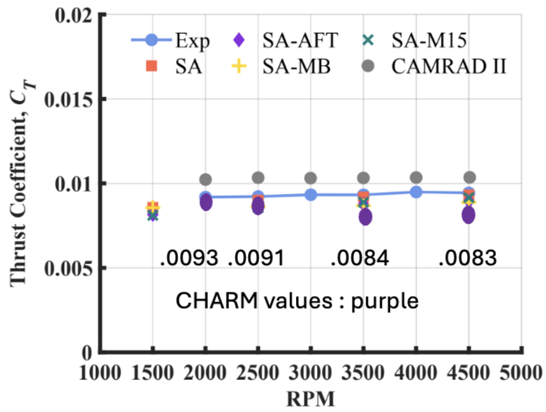

Figure 39: C_T for the Tmotor propeller. CHARM result as purple dot. Experimental value 0.0093.

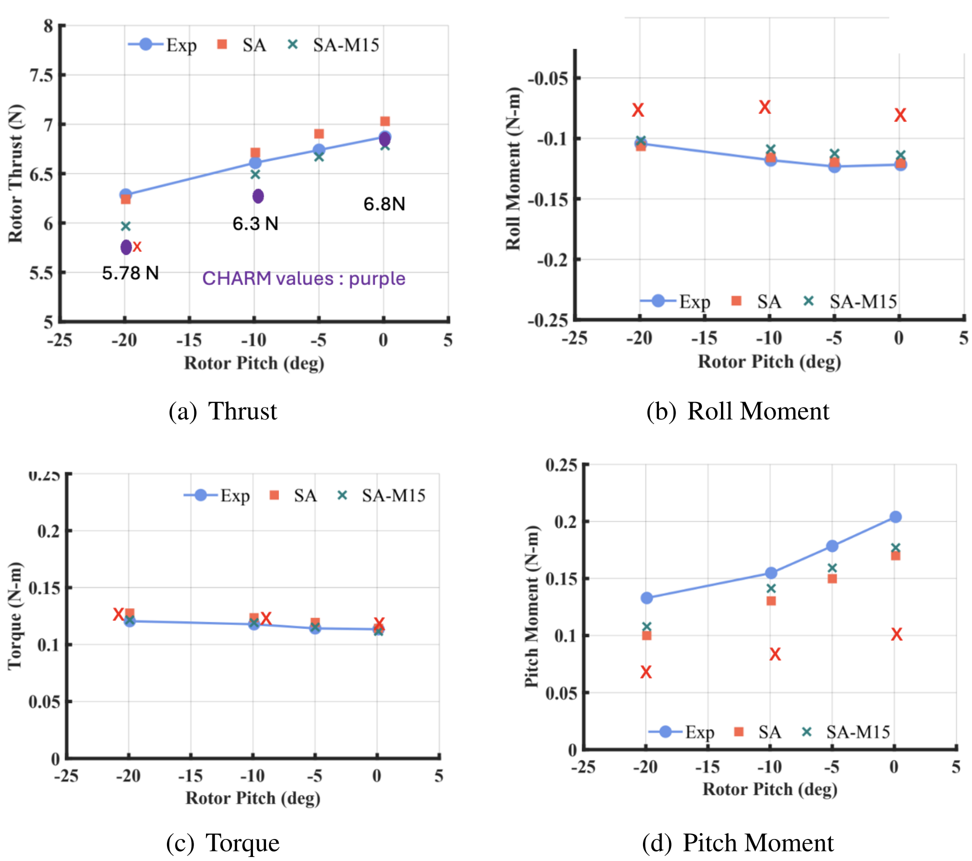

Figure 40: Tmotor propeller 20 ft/s at different tilts CHARM results red X's.

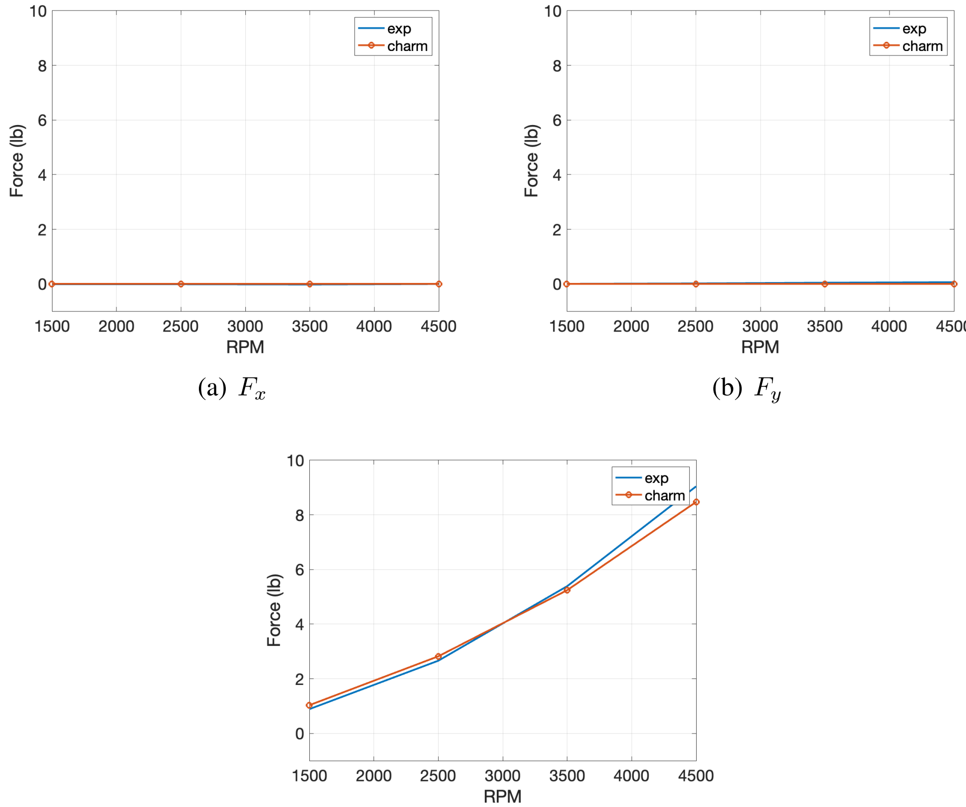

(a) F_x (b) F_y

(c) F_z

Figure 41: SUI hover performance.

moment results are not yet understandable possibly due to necessary coordinate transformations and are not included here.

One case with flow was selected from the NASA report. It is for 20 ft/s flow with the vehicle at a -9.9 deg tilt. The rotors were all run at the same speed for this case. (In another experiment, the rotors' RPMs were chosen to achieve a trim state.) The results for the non-trimmed case are not as favorable as the hover case as seen in Fig. 42 and the increase in error with RPM happens again. Even with a coordinate transformation that may be needed, the results do not change much as 9.9 degrees is rather small as are the F_x and F_y forces.

As we are trying to nail down the performance calculations, no acoustic calculations for the SUI vehicle have been completed yet. Previously, CDI did generate some acoustics results for the single propeller. These will be referred to below in relation to the results we are obtaining for the Joby prop.

Finally, CHARM has been used for preliminary analysis of the Joby prop. The geometry was built using OpenVSP and the OpenVSP2CHARM scripts. After a few iterations on the Joby geometry, the performance trends in hover, perfectly advancing, and perfect edgewise flight have been considered. The geometry used in CHARM is shown in Fig. 43.

We have several airfoil tables related to the Joby prop. Several of the tables include 4 airfoil sections. The sections are shown in Fig. 44. The XFOIL based tables that we generated ourselves have the same 4 section option and also a 23 section option. These are the options that have been considered to date:

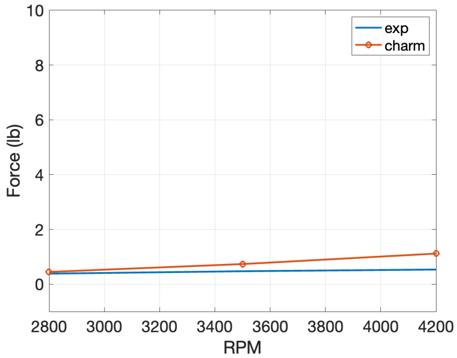

(a) F_x

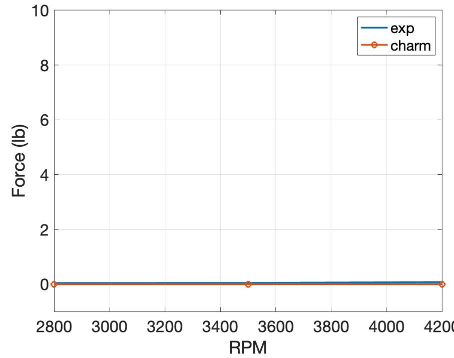

(b) F_y

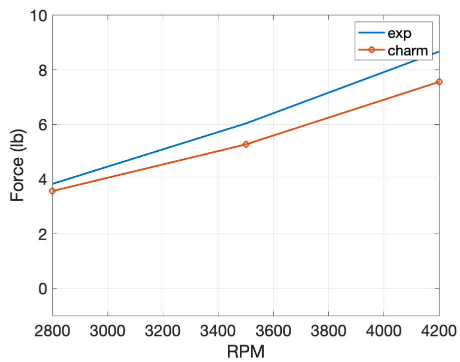

(c) F_z

Figure 42: SUI forward flight performance wind 20 ft/s, tilt -9.9^o- not trimmed.

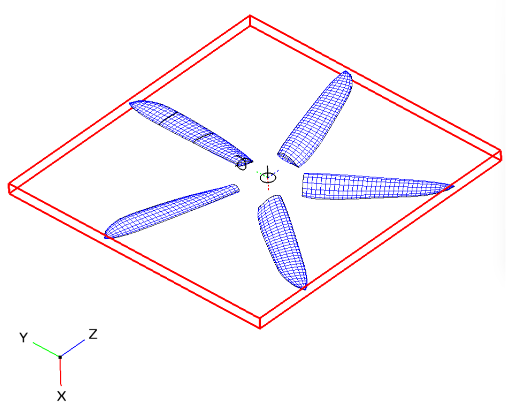

Figure 43: Scaled Joby geometry used in CHARM.

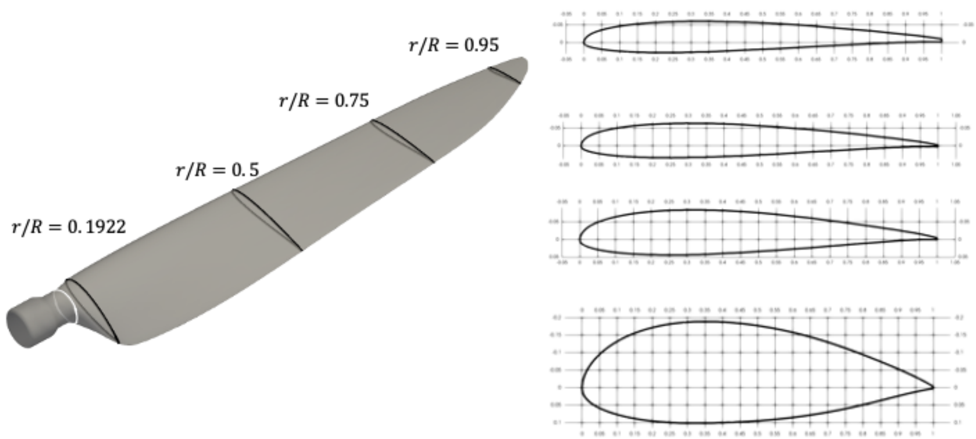

Figure 44: Four locations along Joby blade used for the 4 slice airfoil table.

1) CFD based at RE = 1mil supplied by Joby (4 slices)

2) XFOIL generated at RE = 500k (4 slices, and 23 slices)

3) XFOIL generated at RE = 200k (4 slices, and 23 slices)

4) XFOIL generated at RE = 100k (4 slices, and 23 slices)

Results for the Joby propeller in hover with 16^o pitch at 75% chord are shown in Fig. 45. The effect of changing the airfoil table from 4 sections to 23 sections uniformly decreases the C_T and C_Q. The plots are zoomed in and one can see that the difference between the predictions due to airfoil table selection is on the order of the variance in the experimental results for C_T. It is noted that the actual Reynolds number along the blade remains below 3k as shown in Fig. 46. Based on the previously discussed SUI results, it is doubtful that incorporating the Reynolds number scaling in the CHARM run will change the results significantly. This will be checked in the near future, but we don't expect better agreement.

A forward advancing case was also modeled. Here the inflow is 10 m/s (perpendicular to the propeller plane). Fig. 47 shows that the C_T is a bit low at the higher RPM as was the case for the Tmotor propeller. The C_Q is underpredicted across all of the RPM values. The different Reynolds number airfoil tables do not make a large difference except at the very low RPM.

For the hover case, we have started to consider the acoustics. It was suggested that the overall patterns in the field be considered first as microphone position can be slightly off which makes exact comparison of levels at a specific mic challenging. A regular microphone grid was constructed for use with CHARM. It is shown in Fig. 48. The pattern from the total noise looks more dipolar than what was measured experimentally. It matches the directivity measured however for the Tmotor in hover. Fig. 50 is a plot taken from a CDI report. The experimental data shown on the top was obtained at NASA. The contributions from loading noise and thickness will be explored more thoroughly as well as the effect of using a more accurate thickness geometry file with the WOPWOP calculation.

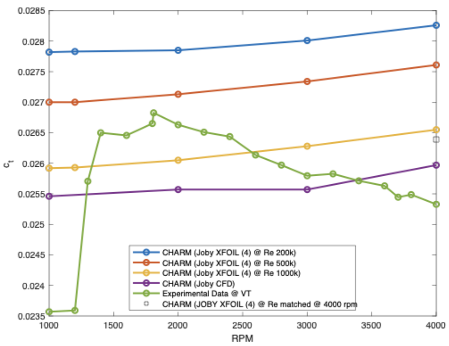

(a) C_T, 4 sections

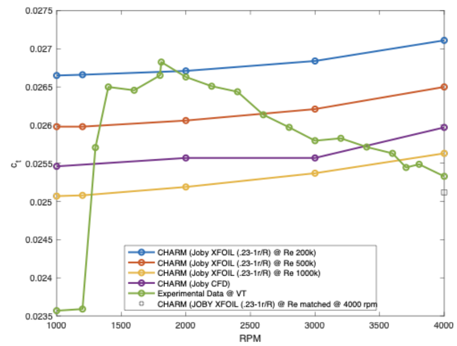

(b) C_T, 23 sections

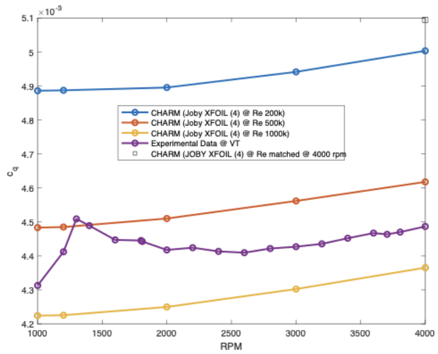

(c) C_Q, 23 sections

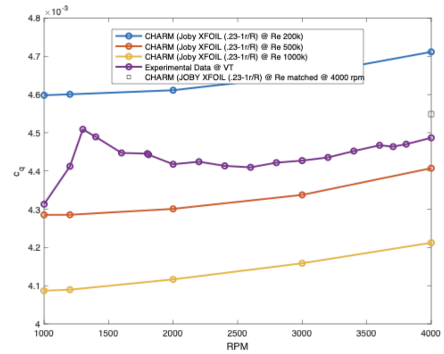

(d) C_Q, 23 sections

Figure 45: Performance of Joby prop in hover from CHARM. Different airfoil tables utilized in calculation.

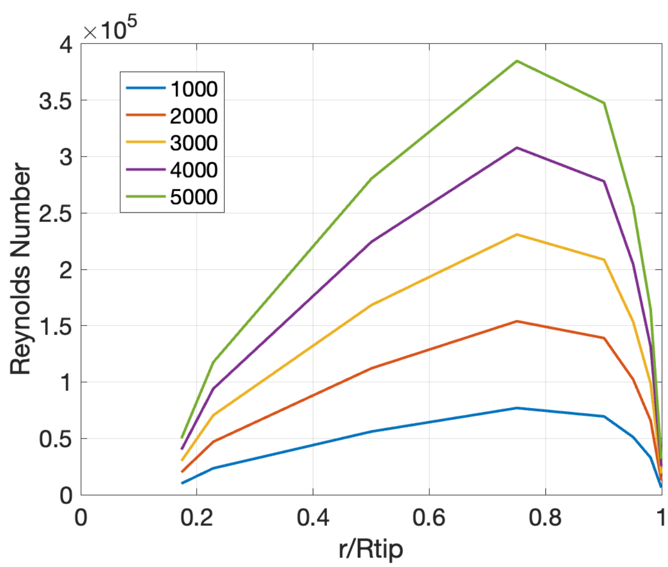

Figure 46: Local Reynolds number along the span of the scaled Joby prop (21% scale) at different RPM.

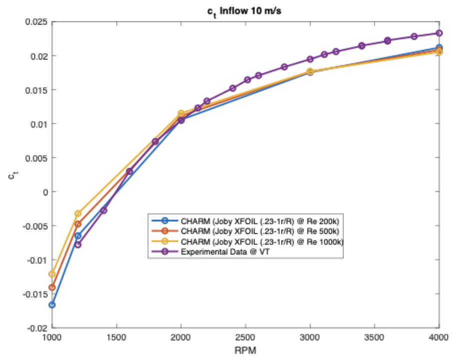

(a) C_T

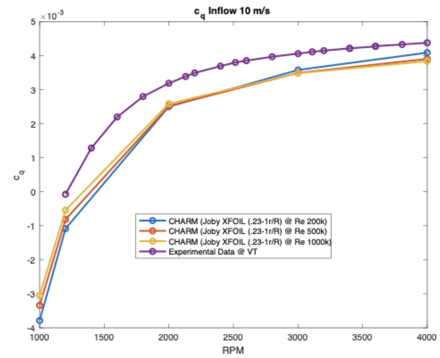

(b) C_Q

Figure 47: Performance of Joby prop advancing at 10/s predicted by CHARM. Airfoil tables generated using XFOIL with 23 slices.

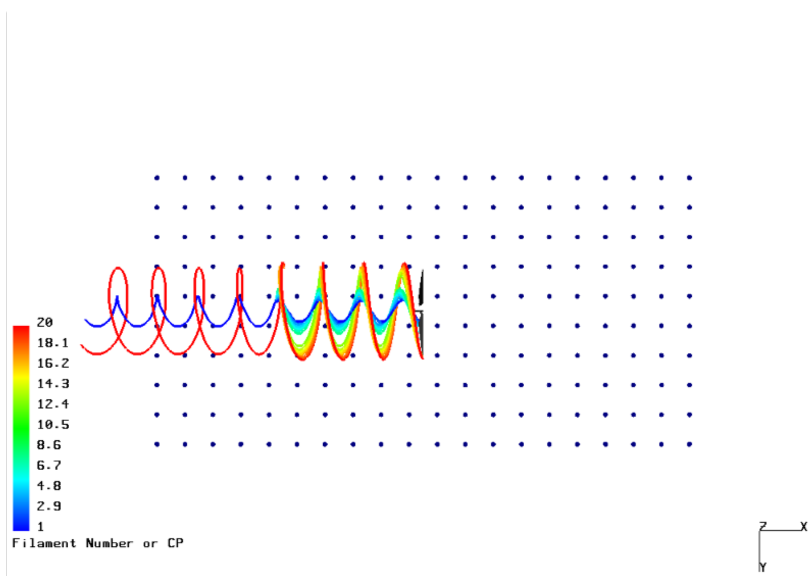

Figure 48: Observer array locations used in CHARM.

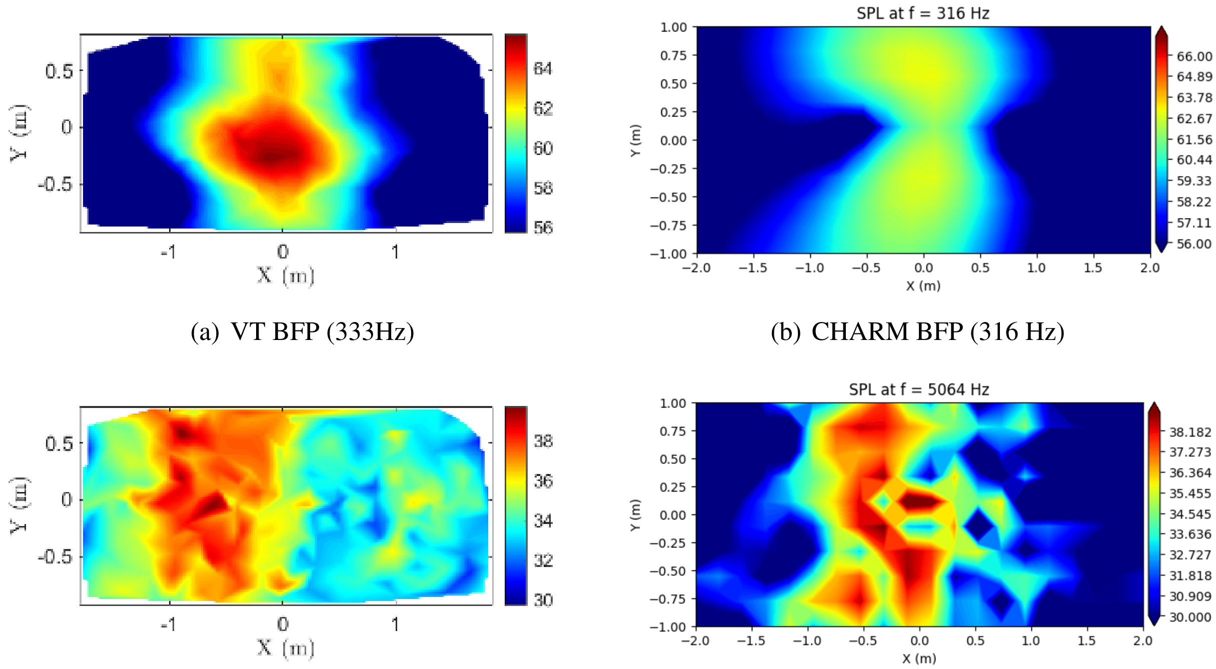

(a) VT BFP (333Hz) (b) CHARM BFP (316 Hz)

(c) VT (5000 Hz) (d) CHARM (5064 Hz)

Figure 49: Joby 3806 RPM.

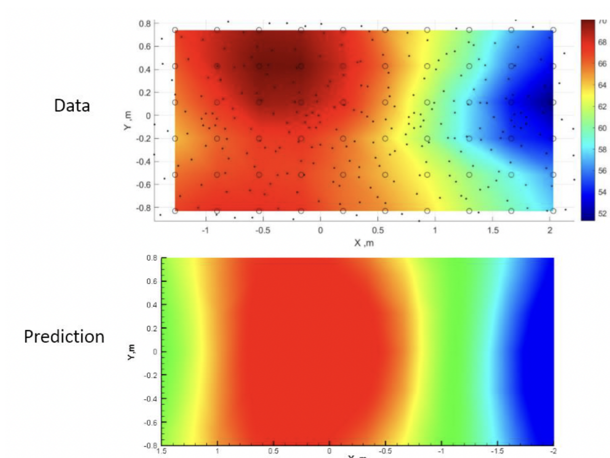

Figure 50: Experimental measurements of and CHARM predicitons of the Tmotor propeller on a plane 1.4m from hub center (0,0). SPL at BPF. Downstream of propeller is to the left.

3.3 Simulation of disturbance interaction with multirotors

The single prop interacting with the wake of the cylinder and fixed wing were discussed in Section 3.2. The Joby propeller with a transient upstream disturbance matching what will be produced at VT will be considered shortly. For the high fidelity computations, now both methods can use overset grids to model the upstream airfoil flap. In CHARM, we believe through imposition of time varying upstream velocity information, the interaction can be simulated. This will be considered in year 2.

Table 6: Milestones and Deliverables for Task 3

Milestone/Subtask /TC/Start-End	**Description (Dependency)**	**Exit Criteria**	**Deliverables**
M3.1/Task 3.1 TC 1,2,3/Q1-5	Validation of high fidelity (M2.3)	Performance to within 5% and noise to within 3dB for tonal and 3 dB OASPL compared to data	Validation test cases and simulation results
M3.2/Task 3.2 TC 1,2,3/Q1-9	Validation of mid and low fidelity (M2.3)	Performance to within 10% and noise to within 3dB for tonal and 3 dB OASPL compared to data	Validation test cases and simulation results
M3.3/Task 3.3 TC 1/Q3-10	Disturbance interaction with multirotors (M1.3,4; M2.4;M3.1,2)	Performance to within 5% and noise to within 3dB for tonal and 3 dB OASPL compared to data	Validation test cases and simulation results

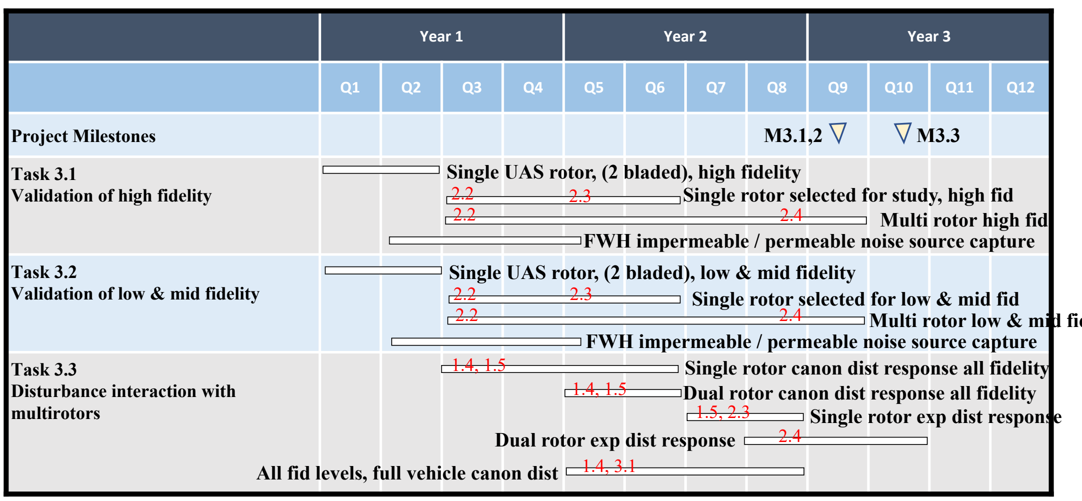

Figure 51: Task 3 schedule. Red indicates required tasks..

4 Multirotor trim prediction

As part of this project, we aim to develop a trim optimization method that will address the nonuniqueness of the trim state for multirotor vehicles. We endeavor to use noise as a control parameter for optimization. Ultimately, we also like to address how the selection of a noise state can work in an unsteady setting. This was the first subtask noted in the proposal but the work is now slated for year 3. Thus we jump to the second subtask.

4.2 Controller for trim optimization given multiple DOF

A controller that can solve a regularized optimization problem to not only achieve the desired trim generalized forces, but also use the redundancy in the control inputs to minimize noise as a secondary cost function, all the while maintaining sufficient safety margins is being developed. This controller will be used both as a real-time controller, and as a computational model for the simulations. For its formulation, we will use the Control Lyapunov Function (CLF)-Control Barrier Function (CBF) framework.[14–18] In a nutshell, this framework uses a local Quadratic Program (QP)[19] at each time step (which can be solved in real time) to find control inputs that (in order of priority from the highest to the lowest): *1)* satisfy safety constraints (e.g., actuator limits); *2)* make progress on the planned route; and *3)* minimize a secondary objective (maximum cumulative noise).

The first step for this task is to provide an explicit characterization of the relation between noise and control inputs in a form that can be used in real-time implementations of the control algorithms.

The second step for this task is to create a controller that can solve a regularized optimization problem to not only achieve the desired trim generalized forces, but also use the redundancy in the control inputs to minimize noise as a secondary cost function, all the while maintaining sufficient safety margins. This controller will be used both as a real-time controller, and as a computational model for the simulations. For its formulation, we will use the Control Lyapunov Function (CLF)-Control Barrier Function (CBF) framework.[14–18] In a nutshell, this framework uses a local Quadratic Program (QP)[19] at each time step (which can be solved in real time) to find control inputs that (in order of priority from the highest to the lowest): *1)* satisfy safety constraints (e.g., actuator limits); *2)* make progress on the planned route; and *3)* minimize a secondary objective (maximum cumulative noise).

In year 1, an important first step was taken. A machine learning approach based on an improved Gaussian Processing method that utilizes gradients was developed and tested on the SUI Endurance quadrotor. The purpose of the machine learning algorithm is to determine the thrust and moment vectors quickly based on basic inputs for the quadrotor such as flight speed and direction and rotor RPM. It will act as a surrogate for BEMT or CFD which can take long times.

The input space of the model is ten-dimensional: four rotor rpm $[r_1, r_2, r_3, r_4]$ and three control angel $[\theta_r, \theta_p, \theta_y]$ (i.e. roll, pitch, and yaw) for aircraft control, wind speed $[v_x, v_y, v_z]$ for environment condition. Together, they form an input $x \in \mathcal{R}^{10}$.

The outputs of this model is six-dimensional: force $[F_x, F_y, F_z]$ and momentum $[T_x, T_y, T_z]$. Merged together, we have the observation of the dynamics as $y \in \mathcal{R}^6$.

Based on the above, we abstracted the quadrotor's kinematic model (i.e., dynamics) into a function f with a 10-dimensional input x and a 6-dimensional output y.

$$f : \mathcal{R}^{10} \to \mathcal{R}^6 \tag{1}$$

The corresponding gradient information is needed. Since we are primarily interested in the impact of control inputs on the dynamics of the aircraft, we focused on calculating the gradients of the 7-dimensional control signals with respect to the 6-dimensional output. These gradient values are combined to form a 6×7 Jacobian matrix:

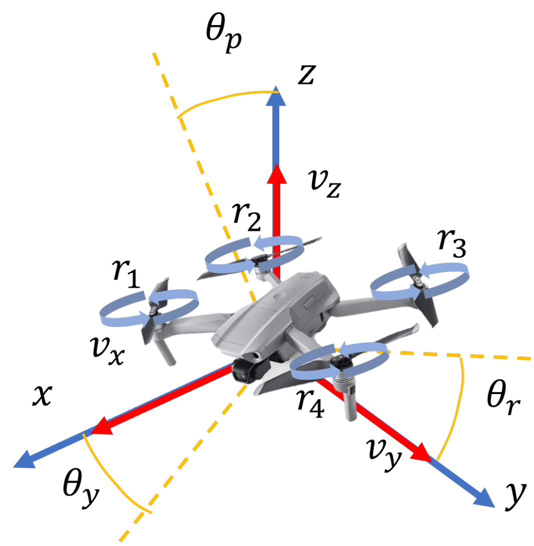

Figure 52: The diagram of every input relative to the quadrotor. The blue arrow indicates the world coordinates. The orange dash line indicates the quadrotor self coordinate.

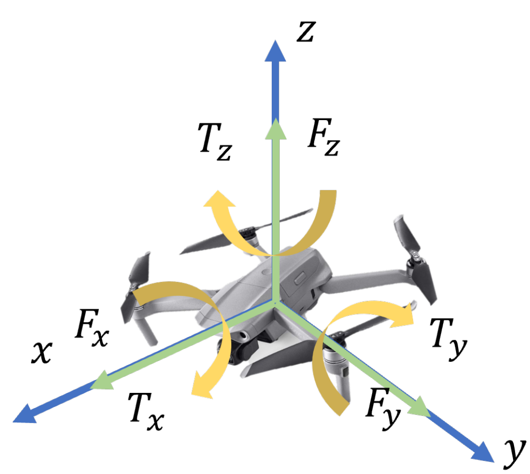

Figure 53: The diagram of every output relative to the quadrotor. The blue arrow indicates the quadrotor coordinate.

$$
\mathcal{J} = \begin{bmatrix}
\frac{\partial F_x}{\partial r_1} & \frac{\partial F_x}{\partial r_2} & \frac{\partial F_x}{\partial r_3} & \frac{\partial F_x}{\partial r_4} & \frac{\partial F_x}{\partial \theta_r} & \frac{\partial F_x}{\partial \theta_p} & \frac{\partial F_x}{\partial \theta_y} \\
\frac{\partial F_y}{\partial r_1} & \frac{\partial F_y}{\partial r_2} & \frac{\partial F_y}{\partial r_3} & \frac{\partial F_y}{\partial r_4} & \frac{\partial F_y}{\partial \theta_r} & \frac{\partial F_y}{\partial \theta_p} & \frac{\partial F_y}{\partial \theta_y} \\
\frac{\partial F_z}{\partial r_1} & \frac{\partial F_z}{\partial r_2} & \frac{\partial F_z}{\partial r_3} & \frac{\partial F_z}{\partial r_4} & \frac{\partial F_z}{\partial \theta_r} & \frac{\partial F_z}{\partial \theta_p} & \frac{\partial F_z}{\partial \theta_y} \\
\frac{\partial T_x}{\partial r_1} & \frac{\partial T_x}{\partial r_2} & \frac{\partial T_x}{\partial r_3} & \frac{\partial T_x}{\partial r_4} & \frac{\partial T_x}{\partial \theta_r} & \frac{\partial T_x}{\partial \theta_p} & \frac{\partial T_x}{\partial \theta_y} \\
\frac{\partial T_y}{\partial r_1} & \frac{\partial T_y}{\partial r_2} & \frac{\partial T_y}{\partial r_3} & \frac{\partial T_y}{\partial r_4} & \frac{\partial T_y}{\partial \theta_r} & \frac{\partial T_y}{\partial \theta_p} & \frac{\partial T_y}{\partial \theta_y} \\
\frac{\partial T_z}{\partial r_1} & \frac{\partial T_z}{\partial r_2} & \frac{\partial T_z}{\partial r_3} & \frac{\partial T_z}{\partial r_4} & \frac{\partial T_z}{\partial \theta_r} & \frac{\partial T_z}{\partial \theta_p} & \frac{\partial T_z}{\partial \theta_y}
\end{bmatrix}
$$

The process for determining a prediction then is

- Stack the data to form matrices that are (d+1)*N by 10 (N being the size of the data set, d is the dimension count with gradient information, 10 is the total state space dimension)
- Compute the covariance of the matrices with the shape of (d+1)*N by (d+1)*N
- Create subsets of the data consist the top 100 data points closest to the new point that is waiting to get dynamics prediction
- Multiply the covariance matrix by a new set of rotor craft state data and obtain the forces and moment vectors

Initial tests comparing traditional Gradient Processing with the enhanced method that utilizes the gradient shows significant accuracy improvement for prediction of the force and moment vectors.

A new database is currently being created with an additional output variable related to the noise. This will change the matrix by adding another row. In year two, the machine learning method will be tested for accuracy in predicting the force and moment vectors as well as the noise parameter.

Table 7: Milestones and Deliverables for Task 4

Milestone/Subtask /TC/Start-End	**Description (Dependency)**	**Exit Criteria**	**Deliverables**
M4.1/Task 4.1 TC 2,3/ Q3-11	Trim in unsteady setting (M2.4,5;M3.3)	Verification across fidelities. Validation within 2% on RPM and 2° on pitch and associated noise to within 3dB OASPL	Verification tests, Validation tests, Insights into effect of trim inclusion on disturbance response
M4.2/Taks 4.2 TC 2,3 / Q6-9	Trim optimizer based on noise metrics (M2.4;M3.2,3)	Demonstrate trim optimization with multiple DOF	Optimization method with newly defined constraints for multi DOF trim

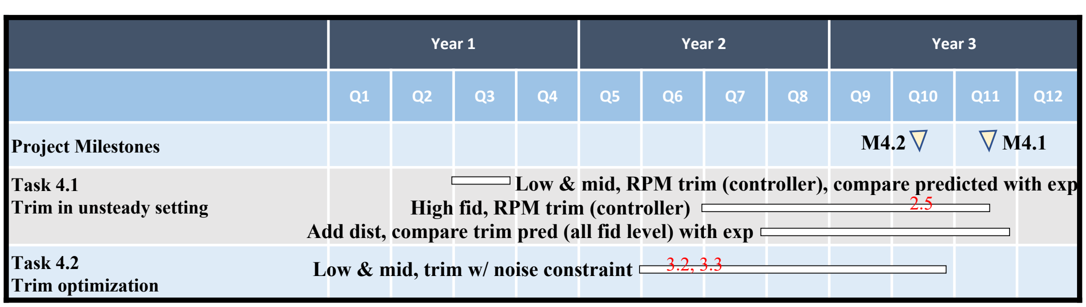

Figure 54: Task 4 schedule. Red indicates required tasks.

5 Safe trajectory planning for UAM

While obstacle avoidance and following reference trajectories are common in path planning, the addition of noise as a constraint represents a new challenge in the field. A new path planning method is being developed. At first, it is assumed that the multirotor and the buildings exist in a no flow environment. In later years, the effect of the real urban flow environment will be considered.

5.1 Path planning algorithm

In year 1, we considered constraints that are defined over accumulated quantities, i.e. functionals of the entire trajectory, as opposed to those that depend solely on the current state as in traditional Higher-order Control Barrier Functions (HOCBF). Then, we demonstrated how RRT* can effectively handle constraints over accumulated quantities - such as total noise or pollution over a path - which are expressed as integral over the entire trajectory. By integrating CBF constraints with RRT, we used the constraints to verify the RRT tree without having to solve Quadratic Programs (QPs). We used a method which comes from the local planner but extends to the RRT tree to extend constraints from individual points to lines and sets by using over-approximations, effectively creating paths that avoid designated zones while still achieving efficient navigation.

This was accomplished by introducing constraints based on integral cost functionals that track an accumulated cost $J(x, t)$ at specific locations x over time t. While we rely on existing HOCBF theory, its application to constraints of the form $J(x, t) \leq J_{\text{limit}}$, where J is a trajectory-dependent integral, is novel. We also introduce a method that saves on computational effort by over-approximating constraints across lines and dense sets, rather than individual points. By setting a Control Barrier Function (CBF) on an upper bound $\bar{J} > J_{\max}$, where $J_{\max}$ is the theoretical maximum value of J over a set, we avoid the need to constantly track $J_{\max}$, significantly reducing computational demands. Together, these contributions allow us to control mobile agents such as quadrotors on paths that are not only void of collisions but also enforce limits on the accumulation of a scalar field such as acoustic noise. To do these, we extended the traditional CBF formulation to encompass constraints that are based on the accumulated effect over time, rather than relying solely on instantaneous state values.

Within the RRT framework, a parabolic kernel is application in order to include noise modeling. This analytical approach allows the RRT* algorithm to efficiently compute the maximal noise impact point q^* and to ensure that the resulting paths do not surpass the noise threshold J_{limit} at any point along the segment. The ultimate objective is to maintain a cost functional less than J_{limit}, preserving the integrity of noise-sensitive regions throughout the robot's trajectory.

Figure 55(a) shows the result of the simulation using the QP with only the obstacle CBF constraints. In the figure, the trajectory's goal is symbolized by a green star while the starting position is shown in orange, and it is observable that the quadrotor maintains a safe distance from the obstacle towards the goal, adhering to established safety measures. Since this simulation does not take into account the constraint $J(t) < J_{\text{limit}}$, while the quadrotor effectively avoids the specified physical obstacles, it may exceed the allowable cumulative impact at certain locations.

Figure 55(b) shows the quadrotor navigating toward its goal, detouring upon encountering an obstacle. The escalating noise around this obstacle prompts the quadrotor to maintain distance, thereby steering clear of the accumulating noise while persistently moving toward its target.

For the RRT*, without noise constraints, the simulation shows the robot's path maneuvering between the obstacles to reach its destination, which is shown in Figure 56(a). When a the noise

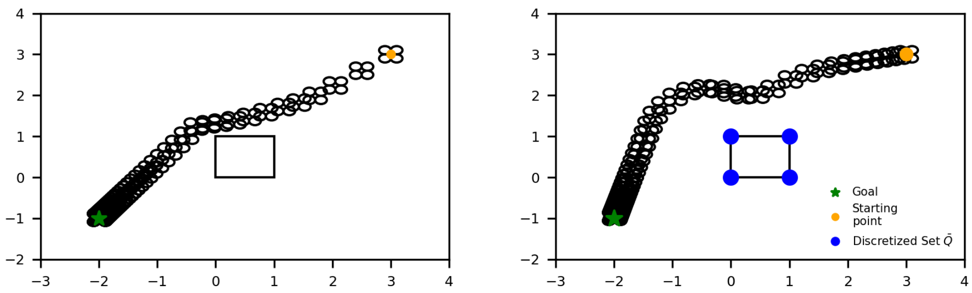

(a) Trajectory without Noise Constraint (b) Trajectory with Noise Constraint

Figure 55: Comparison of Trajectories with and without Noise Constraints

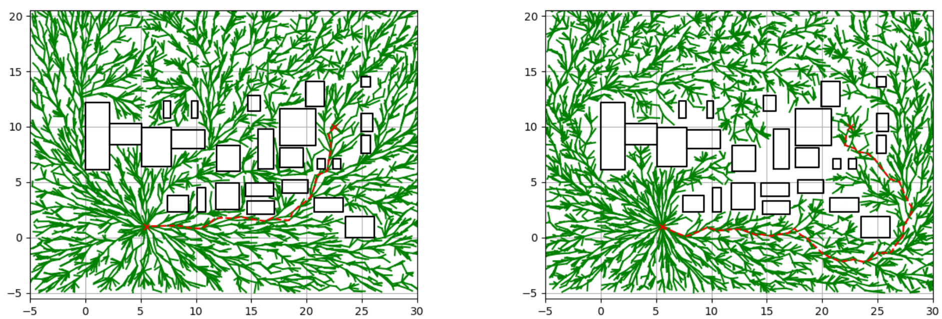

(a) RRT* Trajectory without Noise Constraint (b) Trajectory with Noise Constraint

Figure 56: Comparison of RRT* Trajectories with and without Noise Constraints

constraint is introduced ($J_{\text{limit}} = 10$) the robot alters its trajectory asseen in in Figure 56(b). In the simulation, the robot will avoids going in-between obstacles choosing a safe path that doesn't go beyond the noise limit. As the noise spreading factor is increased, simulations also show that the radius of the path the robot takes around the corner of the building increases.

The noise was modeled here based on a very simple amplitude decay function with distance from the quadrotor. The quadotor was also simply modeled as a single entry with no noise source distribution. Finally, the buildings were treated as transparent rather than reflective and absorptive entities. Evolving to more realistic models is planned for Year 2. This will require a decision as to the best noise parameter(s) to use for path planning Examples of possible noise constraints include the total area with LAmax above 65dB, LAmax at specific location, or time above 65 dBA at specific locations. Other path planning objectives may include minimum time and minimum energy usage. Given the flexibility afforded by our controller and path planning algorithm, it will be feasible to assess the changes in optimal trajectories caused by different acoustic and performance tradeoffs.

Table 8: Milestones and Deliverables for Task 4

Milestone/Subtask /TC/Start-End	Description (Dependency)	Exit Criteria	Deliverables
M5.1/Task 5.1 TC 3/Q5-8	Extend controller (M4.1)	Demonstrate cumulative and area constraints	Improved CLF-CBF algorithm
M5.2/Task 5.2 TC 3/Q4-8	Path planning algorithm (M3.3)	Demonstrate simulation of diff path outcomes due to diff noise constraints	Extended RRT* algorithm
M5.3/Task 5.3 TC 3/Q8-12	Path planning w/ & w/o urban flow (M1.3;M3.3;M4.3)	Demonstrate path planning through Boston model	Simulation results. Method details.

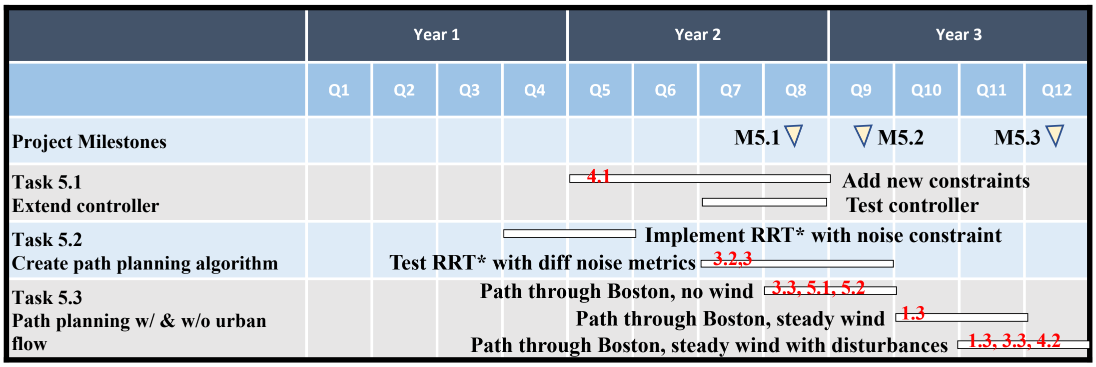

Figure 57: Task 5 schedule. Red indicates required tasks.

5.2 Path planning with and without urban flow - Planned for Year 3

Education/workforce development

A workshop was held on the campus of Virginia Tech May 20-24, 2024 with the aim to showcase research relevant to UAM and UAS to underrepresented students in engineering. These students were predominantly rising undergraduate seniors from other academic institutions. Recruitment focused on schools without graduate programs and schools that have a high number of minority students enrolled in ENG. One objective of this program was to highlight the opportunities available for students in graduate school so that they would apply to Virginia Tech or other graduate programs. This workshop included multiple relevant lab tours and a field trip to the Wing nest located in Christiansburg, VA. The participants heard from many guest speakers as well as faculty from the partner institutions: BU, ERAU, and Tuskegee. Members of the advisory board were also present in Blacksburg or virtually for a review of the project's progress. In total, the workshop hosted 19 undergraduate participants for the entire week, 9 graduate students supported by the ULI, 6 ULI faculty members, 10 guest speakers, and 3 in-person and 2 online members of the advisory panel. Students were led through the process of predicting aerodynamic performance and noise. In addition, they programmed drones and flew them through an obstacle course. Guest speakers included representatives from Whisper Aero, Joby Aviation, Wing, and the Mid-Atlantic Aviation Partnership. Figure 11 shows a picture of the undergraduate participants during their visit to the Wing nest.

Joby hosted four interns affiliated with the NASA ULI program during the summer of 2024. Michael Marques (ERAU, PhD, 2025),Fig. 59(a), worked with the acoustics team applying the research under the ULI to the Joby propeller tested at the National Full-Scale Aerodynamics Complex (NFAC). This work will be documented in a technical paper at an upcoming AIAA

Figure 58: Students visiting the Wing nest in Christiansburg, VA.

conference. Renato Korzinek (BU, BS 2025), Fig. 59(b) also worked with the experimental data from the NFAC test for the rotor dynamics team. He worked on automating the plotting and comparing the test results to various computational analysis methods to better understand the utility of different models. Kent Liao (BU, BS 2025), Fig. 59(c) worked with loads team to compare the predicted mass properties with the actual aircraft built on its Pilot Production Line. Ryan Lundquist (VT, MS 2024), Fig. 59(d) worked with the Modeling and Simulation team to implement an improved atmospheric turbulence model into the Integrated Vehicle Simulator (IVS) used in a wide variety of testing. All the interns took trips to other Joby facilities in San Carlos and Marina, CA. The internships were a valuable experience for the interns. These students will now continue their ULI research which will now be highly informed by their internship experience and their deeper knowledge of the Joby aircraft.

(a) Michael Marques

(b) Renato Korzinek

(c) Kent Liao

(d) Ryan Lundquist

Figure 59: Joby summer 2024 interns.

References

[1] B. Maronga et. al. Overview of the palm model system 6.0. *Geoscientific Model Development*, 2020.

[2] T. S. Lund, X. Wu, and K. D. Squires. Generation of turbulent inflow data for spatially developing boundary layer simulations. *J Comput Phys*, 40:233–258, 1998.

[3] S. Huang, Q. Li, and J. Wu. A general inflow turbulence generator for large eddy simulation. *Journal of Wind Engineering and Industrial Aerodynamics*, 98(10-11):600–617, 2010.

[4] A. Stoll and J Bevirt. Development of evtol aircraft for urban air mobility at joby aviation. In *VFS AHS 78th Annual Forum*, 2022.

[5] A. S Hersh, P. T. Soderman, and R. E. Hayden. Investigation of acoustic effects of leading-edge serrations on airfoils. *J. Aircraft*, 11(4):197–202, 1974.

[6] P. Vadher and H. Babinsky. Experimental generation and characterization of isolated vortical gusts. *AIAA Paper No. 2023-0050*, 2023.

[7] UniCFDLab. Unicfdlab: libacoustics library for far-field noise computation. `https://github.com/unicfdlab/libAcoustics`. Accessed: 2020.

[8] A. Thai and S. Grace. Prediction of small quadrotor blade induced noise. *AIAA Paper No. 2019-2684*, 2019.

[9] Y. Yauwenas, J. R. Fischer, D. Moreau, and C. J. Doolan. The effect of inflow disturbance on drone propeller noise. *AIAA Paper No. 2019-2663*, June 2019.

[10] APC. Apc propeller performance data. `https://www.apcprop.com/technical-information/performance-data/`. Accessed: 2023.

[11] O. D. Dantsker, M. Caccamo, R. W. Deters, and M. S. Seli. Performance testing of apc electric fixed-blade uav propeller. *AIAA Paper No. 2022-4020*, 2022.

[12] Z. Czyz, P. Karpinski, K. Skiba, and M. Wendeker. Wind tunnel performance tests of the propellers with different pitch for the electric propulsion system. *Sensors*, 20(2):1–18, 2022.

[13] Carl Russell, Gina Willink, Colin Theodore, Jaewoo Jung, and Brett Glasner. Wind tunnel and hover performance test results for multicopter UAS vehicles. Technical Report TM—2018–219758, NASA, 2018.

[14] Aaron D Ames, Xiangru Xu, Jessy W Grizzle, and Paulo Tabuada. Control barrier function based quadratic programs for safety critical systems. *IEEE Transactions on Automatic Control*, 62(8):3861–3876, 2017.

[15] Mrdjan Jankovic. Robust control barrier functions for constrained stabilization of nonlinear systems. *Automatica*, 96:359–367, 2018.

[16] Ian R Petersen and B Ross Barmish. Control effort considerations in the stabilization of uncertain dynamical systems. In *IEEE American Control Conference*, pages 490–495. IEEE, 1984.

[17] Aaron D Ames, Kevin Galloway, Koushil Sreenath, and Jessy W Grizzle. Rapidly exponentially stabilizing control lyapunov functions and hybrid zero dynamics. *IEEE Transactions on Automatic Control*, 59(4):876–891, 2014.

[18] Eduardo D Sontag. A ‘universal’construction of artstein’s theorem on nonlinear stabilization. *Systems & control letters*, 13(2):117–123, 1989.

[19] S.P. Boyd and L. Vandenberghe. *Convex optimization*. Cambridge University Press, 2004.